TÉCNICO LISBOA

Characterization of Inverse Diffusion Flames with Methane and Hydrogen

Francisco Maria Machado Rosa Neves Vaz

Thesis to obtain the Master of Science Degree in

Mechanical Engineering

Supervisors: Prof. Edgar Caetano Fernandes
Eng. Filipe João Marques Quintino

Examination Committee

Chairperson: Prof. Carlos Frederico Neves Bettencourt da Silva
Supervisor: Prof. Edgar Caetano Fernandes
Members of the Committee: Dr. Ana Filipa da Silva Ferreira
Prof. Teodoro José Pereira Trindade

December 2019

Dedico este trabalho à minha Mãe, Margarida, ao meu Pai, Carlos, e aos meus irmãos, Henrique e João.

Agradecimentos

Esta tese é o culminar de um longo e importante caminho que, felizmente, não foi feito sozinho. Neste espaço, presto os devidos agradecimentos e reconhecimentos a quem mais me ajudou nesse mesmo caminho.

Em primeiro lugar, quero agradecer aos meus supervisores. Ao professor Edgar Fernandes pela oportunidade que me concedeu e por toda a sua visão, entusiasmo e motivação, que foram fundamentais para a conclusão deste trabalho. Ao Filipe Quintino, por toda a sua entrega e profissionalismo com que abordou este trabalho. A sua imensa sabedoria e persistência na procura da excelência foram determinantes na execução deste trabalho.

Agradeço ao professor Mário Costa e ao Sr. Manuel Pratas a disponibilização dos analisadores de gases e do uso do laboratório de combustão do IDMEC, fundamentais para a realização deste trabalho.

Deixo também uma importante palavra de agradecimento aos meus colegas de trabalho, Miguel Ribeiro, Alexandre Gamboa, Miguel Santos, Mafalda Medeiros, Muhammad Raiyan e Miguel Fechado por toda a ajuda que me prestaram nesta tese.

Agradeço também aos meus grandes amigos da faculdade, Tiago Oliveira, Francisco Brás Monteiro, Francisco Bertão, Luís Fialho, Francisco Vieira e José Rajani por todo o acompanhamento.

Quero deixar o mais profundo agradecimento à minha família: aos meus avós e às minhas primas Leonor e Marta por todo o seu apoio e genuíno interesse no meu trabalho. Especialmente, aos meus pais e irmãos, a quem devo tudo, pelo seu apoio incondicional.

À Catarina, que foi quem mais me apoiou neste percurso.

This work was developed at the Thermofluids, Combustion and Energy Systems laboratory of the IN+ - Center for Innovation, Technology and Policy Research.

Resumo

O impacto das emissões de gases de efeito de estufa nas alterações climáticas tem vindo a pressionar a indústria da combustão para encontrar novas soluções, mais limpas e eficientes. As chamas de difusão inversa (IDF) combinam as vantagens das chamas de difusão convencionais e de pré-mistura, exibindo uma abrangente gama de estabilidade na queima de misturas pobres e pouca produção de fuligem. O hidrogénio, por sua vez, quando misturado com um hidrocarboneto convencional, pode melhorar significativamente a qualidade da combustão e reduzir as emissões. Nesta tese é feito um estudo experimental sobre o impacto da proporção de hidrogénio na mistura de combustível, na estrutura e emissões de uma IDF com metano, num queimador de secção retangular, em condições de mistura pobres. Foram testados combustíveis com 0%, 25% e 50% de H_2, a razão de equivalência global foi variada de 0.2 a 1.0 e a potência de chama foi mantida a 236 W. Foi feita uma análise de PIV (Particle Image Velocimetry) e medidas a emissões de UHC, CO, CO_2 e NO_x. Foram identificados dois tipos de estrutura de chama (Tipo I e II). O hidrogénio não criou novas estruturas mas afetou as gamas de estabilidade de I e II. A análise de PIV revelou uma grande fração do jato de ar que não participa na combustão, na chama Tipo II. Percebeu-se que a eficiência depende do tipo de chama, sendo que esta é maior no Tipo I. A adição de hidrogénio reduziu as emissões de espécies que contêm carbono para ambas as estruturas e de NO_x para I, sendo que estas aumentaram para II. O hidrogénio permitiu estabilizar a chama I em condições mais pobres.

Palavras-chave: Chama de Difusão Inversa, Hidrogénio, Emissões, NO_x, PIV

Abstract

Greenhouse gas emissions and their climate impact are forcing the combustion industry to devise clean and more efficient solutions. Contrary to conventional flame configurations, Inverse Diffusion Flames (IDF) combine benefits of premixed and diffusion flames, exhibiting extended lean flammability range and low soot production. Hydrogen, in turn, when blended with hydrocarbon-based fuels, can significantly enhance combustion processes and reduce emissions due to its unique properties. In this thesis, an experimental study was conducted to assess the impact of H_2 enrichment on the flame structure and emissions of a methane IDF in a multi-slit rectangular burner, under fuel-lean conditions. Fuel blends containing 0%, 25% and 50% H_2 were tested, the global equivalence ratio was varied between 0.2 and 1.0 and flame power fixed at 236 W. A PIV (Particle Image Velocimetry) analysis was performed and measurements of the CO_2, CO, UHC and NO_x emissions were attained. Two distinct flame structures were identified (Type I and II). It was found that H_2 addition does not create new flame structures but affects the stability range of Type I and II. PIV analysis demonstrated that a significant fraction of the central air jet escapes combustion in flame structure II. Efficiency was found to be dependent on flame structure, with Type I exhibiting better performance overall. Hydrogen enrichment lowered carbon-related emissions for both flame structures and reduced NO_x for flame Type I whereas the opposite was found for flame Type II. Finally, hydrogen enabled to maintain flame structure Type I for leaner conditions.

Keywords: Inverse Diffusion Flame, Hydrogen, Emissions, NO_x, Particle Image Velocimetry

Contents

List of Tables

List of Figures

Nomenclature

Acronyms

1D One-dimensional.

2D Two-Dimensional.

CAP Circumferentially Arranged Ports.

CCD Charged Coupled Device.

CoA Co-annular.

FRA Flame Region A.

FRB Flame Region B.

IA Interrogation Area.

IDF Inverse Diffusion Flame.

LHV Lower Heating Value.

LPG Liquefied Petroleum Gas.

NDF Normal Diffusion Flame.

PIV Particle Image Velocimetry.

PLIF Planar Laser Induced Fluorescence.

RMSE Root Mean Square Error.

SLPM Standard Litter Per Minute.

STP Standard Temperature and Pressure.

UHC Unburned Hydrocarbons.

Chemical species

CH_4 Methane.

CH Methylidyne radical.

CO_2 Carbon dioxide.

CO Carbon monoxide.

H_2O Water.

H_2 Hydrogen molecule.

N_2 Nitrogen molecule.

NO_x Nitrogen oxides.

O_2 Oxygen molecule.

Pt Platinum.

Rh Rhodium.

Greek symbols

χ Volumetric fraction.

μ Viscosity.

ν Kinematic viscosity.

ϕ Global equivalence ratio.

ρ Density.

Roman symbols

A Area.

a Stoichiometric coefficient of oxygen for complete fuel combustion.

D Diameter.

e Relative error.

E_I Emissions of flame Type I.

E_{II} Emissions of flame Type II.

EI_i Emission Index of species i.

O_i Observed.

P_i Predicted.

Δh_c Heat of combustion.

L Length.

l Length of the burner.

m Mass.

MW Molecular Weight.

P Power.

$\dot{Q}$ Volumetric flow rate.

Re Reynolds number.

Δt Time between pulses.

$\overline{U}$ Average Velocity.

U Velocity; uncertainty.

V Velocity.

w Width of the burner.

x Volumetric fraction.

x, y, z Cartesian coordinates.

y Molar fraction.

Subscripts

f Fuel.

h Hydraulic.

m Measured.

max Maximum.

r Ratio.

st Stoichiometric conditions.

Superscripts

TM Trademark.

Chapter 1

Introduction

1.1 Motivation

1.1.1 Inverse Diffusion Flames

The impact of greenhouse gases on global warming [1] and the fast pace at which energy demand is increasing [2] are imposing the energy industry to reinvent itself. Notably, energy systems are striving to be cleaner and more efficient. According to the BP Energy Outlook of the present year [3], the share of oil, gas and coal altogether, in primary energy consumption, by the year 2040, may be about less than 30% of what it is now. On the other hand, the correspondent renewables'[1] share might just to step up from 4%, now, to 29%, in 2040. Furthermore, with the escalating consumption of primary energy, investments towards more efficient energy systems are a major concern today - the International Energy Agency (IEA) [4] estimates a total of USD 240 billion invested in energy efficiency across the buildings, transport, and industry sectors in 2018. Figure 1.1 depicts a forecast of the total primary energy demand in a sustainable development scenario [2], with carbon based fuels decreasing in demand, in contrast to the growing clean energy sources. These statistics, and many others, are forcing the combustion industry to find new solutions, in order to compete with the arising alternatives in terms of clean and efficient energy production.

In this context, a flame configuration different from the traditional premixed and normal diffusion configurations has been captivating more attention over the last few years - the Inverse Diffusion Flame (IDF). It is a diffusion flame because its reactants are initially separated. However, as it name suggests, the fuel-oxidizer configuration is inverted. Whereas in a Normal Diffusion Flame (NDF), a fuel jet is typically immersed in an oxidizing atmosphere [5], in the case of IDF, there is a central air jet surrounded by fuel. In spite of being a diffusion flame, it features a central air jet, usually with much higher velocity than that of the surrounding fuel. This velocity gradient, with higher velocities of the central air jet, creates a negative pressure difference towards the center that will entrain the surrounding fuel jets and some ambient air [6]. This fuel entrainment, in turn, will promote a premix of air and fuel, possibly resulting in a blue appearance flame, especially if the Reynolds number of the central air jet is much

[1] Renewables includes wind, solar, geothermal, biomass, and biofuels.

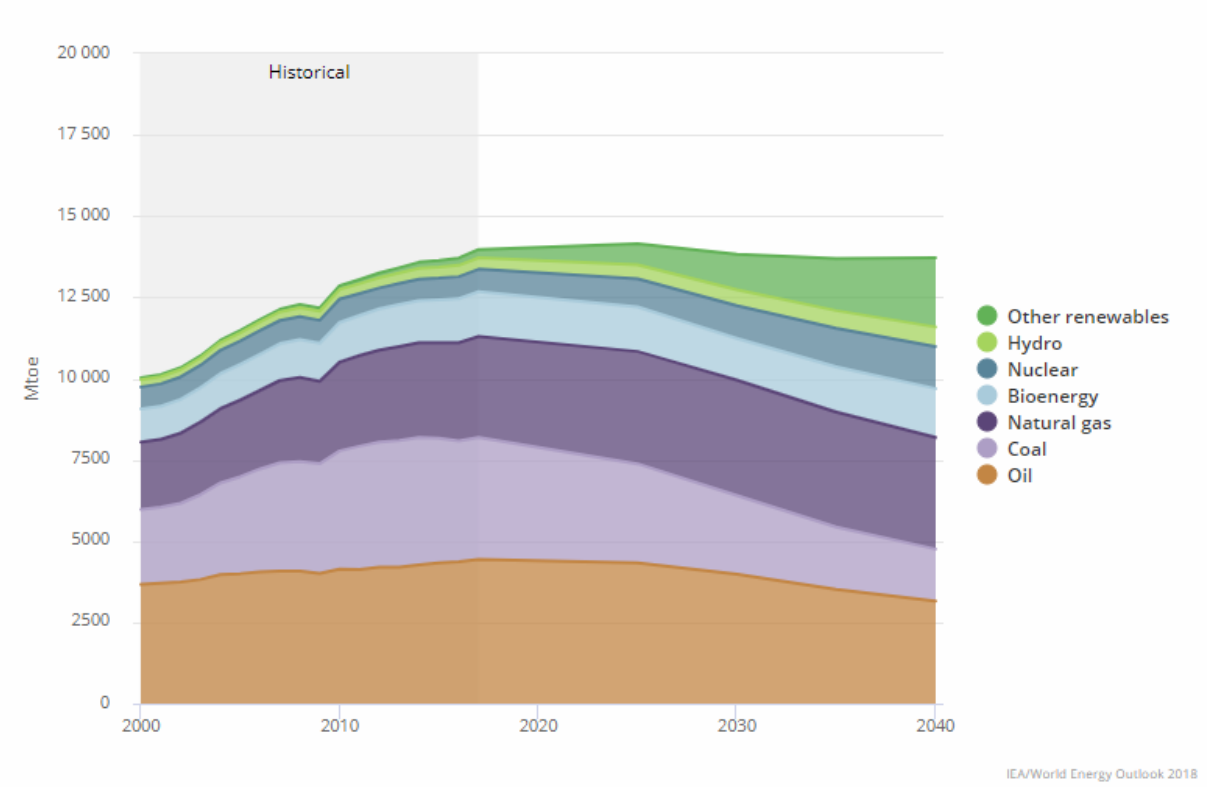

Figure 1.1: Forecast of the total primary energy demand in a sustainable development scenario. Source: [2].

higher than that of the adjacent fuel [6, 7]. Therefore, this flame configuration combines the nature of NDFs and premixed flames, to form a flame that may have the advantages of both: wide range of stability and no risk of flashback, in the case of NDFs, plus low pollutant emissions and high efficiency, in the case of premixed flames [7, 8].

1.1.2 Hydrogen

Hydrogen is the most abundant element in the universe. However, it mostly is in the form of water or organic compounds. Therefore, to obtain pure hydrogen, H_2, one needs to spend energy, mainly on processes like natural gas reforming or electrolysis. Due to its potential as an energy carrier, hydrogen has been receiving much consideration for energy storage purposes [9, 10]. The low capacity factors of renewables and its intermittent nature are forcing them to find new solutions to store the excess electricity produced in off-peak hours. Using that extra power to feed electrolysis, thus producing hydrogen, is a possible solution that has been earning interest.

Furthermore, hydrogen has great thermal and molecular diffusivity, high burning speed and low ignition energy [11–14]. When added to other fuels, it may increase flame temperature and enhances the heat release rate [15, 16]. Since it has no carbon, theoretically, its combustion leaves only water vapor behind, making it attractive as a possible substitute for carbon based fuels. A viable way of taking advantage of these hydrogen properties is to burn it along with a traditional hydrocarbon fuel [17, 18].

Hydrogen's unique properties and a possible positive trend in hydrogen production in a near future foster

new investigations regarding combustion of hydrocarbons enriched with hydrogen fuel.

1.2 State of the Art

1.2.1 Inverse Diffusion Flames

First studies of IDF featured the traditional co-annular burner, with an interior air channel and a surrounding concentric annular fuel channel as depicted in Figure 1.2 (a). Inception of IDF's investigations date back to 1955, with Arthur and Napier [19] assigning stronger luminosity and soot formation to NDFs when compared with IDF. In 1984, Wu and Essenhigh [20, 21] classified IDF into six different types, based on six different regimes in terms of flame stability and appearance. More recently, Shaddix et al. [22] denoted less soot production in IDF than in NDF, however, the latter exhibited less instabilities. Following Shaddix's studies, Mikofski et al. [23–25] studied the effect of the Reynolds number of the central air jet (Re_{air}) on IDF height and structure, pointing out a double flame structure with a partially premixed flame base, followed by a normal diffusion regime with higher levels of soot production.

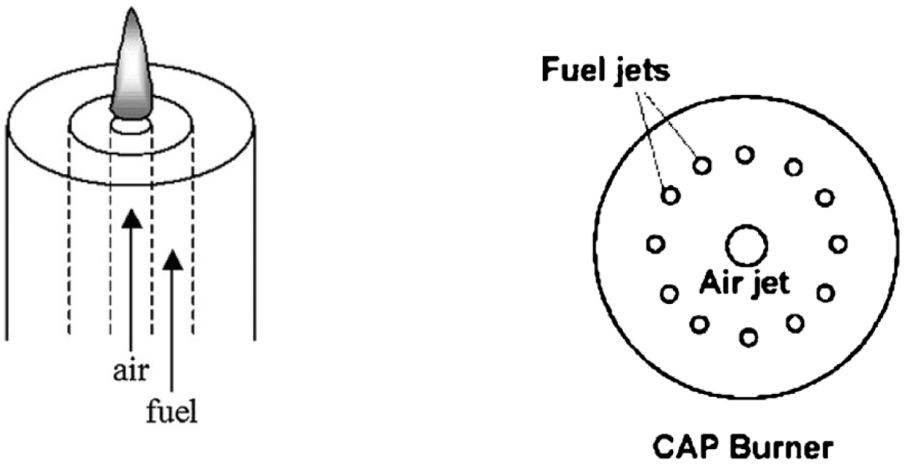

(a) CoA burner. Source: [25].

(b) CAP burner. Source:[26].

Figure 1.2: Co-anullar burner (CoA) and burner with circumferentially arranged fuel ports (CAP).

In spite of several interesting results with the CoA burner, in the last fifteen years, a burner configuration with Circumferentially Arranged fuel Ports (CAP), has been deserving more consideration. Figure 1.2 (b) illustrates the CAP burner configuration with an outer circumference where the fuel ports sit and with an inner larger port for air.

Regarding flame structure and stability analysis with CAP burners, Sze et al., followed by others [6, 7, 26–28], reported improved flame stability and reactants mixing due to significant fuel entrainment by the central air jet. Dong et al. [7, 27] argued that flame structure is mainly dependent on Re_{air} and velocity ratio between air and fuel ($V_r = V_{air}/V_{fuel}$), reporting a very wide range of stable IDF in terms of these two variables. A dual structure flame was identified, with a flame base and a flame torch similar to a premixed flame, connected by a "neck like" structure with flow recirculation. This dual flame structure was also reported by Elbaz and Roberts with methane fuel [29]. Zhen et al. [30] reported that a shorter

nozzle length enhances reactants mixing leading to faster and more complete combustion and reduces the height of the flame base. It was found by [31] that smaller diameter of the central air port may lead to more bluish flames, with improved air-fuel mixing, higher temperatures and wider stability range in terms of Re_{air} and V_r. Swirling IDF were studied also by Zhen et al. [32, 33] showing that swirl improves stability and heat transfer rates. Most of these studies were based on Liquefied Petroleum Gas (LPG) as a fuel [6, 7, 26, 27, 30–33].

Considering now studies regarding temperature and emissions of IDF, most of them also featured a CAP burner. Actually, Sze et al. [26] started by comparing NO_x emissions of IDF in CAP and CoA burners, showing maximum NO_x emissions in CAP burners for near stoichiometric conditions, whereas in CoA burners, maximum NO_x emissions showed up in richer conditions. Temperatures of IDF in both burners exhibited similar values [26]. Further studies regarding temperature and emissions would be resumed by [7], with maximum temperature measurements pointing to values lower than 1800 K for lean conditions and exhibiting small dependency on Re_{air} for fixed velocity ratios. However, temperature was highly dependent on the location within the flame, as it would be expected since IDF is a diffusion flame. NO_x emissions increased with ϕ due to temperature increase while CO exhibited and opposite trend. Zhen et al. [30] would later verify that short nozzle lengths, due to faster combustion, result in higher temperatures and higher CO_2 and CO emissions. Decreasing the diameter of the air port, d_{air}, was proven to have an impact in emissions from IDF [31], increasing CO and HC emissions due to shorter residence times and decreasing NO_x emissions due to lower volume of high temperature zones.

Recently, Ribeiro et al. [34] performed an extensive study in a multi-slit burner: it has three rectangular channels with equal dimensions, represented in Figure 1.3. The lateral rectangular slits are for fuel, whereas the central one is for air. The analysis by Ribeiro et al. used methane as fuel and focused on

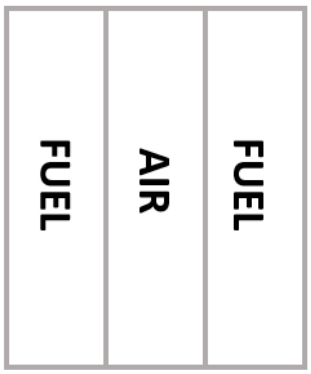

Figure 1.3: Schematic top view of the multi-slit rectangular burner.

characterizing the IDF morphology. With a constant power supplied to the flame, V_r was varied by varying V_{air}. Chemiluminescence and Particle Image Velocimetry (PIV) analysis were performed, in order to understand the local variations of the equivalence ratio and the velocity field of the flames studied, respectively. Mainly three flame types were studied, with different global equivalence ratios[2] (rich: low V_r,

[2]Global equivalence ratio is dictated by the relative amounts of air and fuel supplied to the flame. Section 2.1.2 provides an important remark about the difference between global and local equivalence ratios throughout this text.

stoichiometric: intermediate V_r and lean: high V_r) that resulted in three different morphologies, shown in Figure 1.4. The rich flame type presented some soot production in contrast to the remaining two types. The lean flame presented a "neck-like" structure [7]. V_r showed great impact on flame structure, with higher velocity ratios resulting in enhanced mixing of air and fuel due to higher fuel entrainment by the air jet. The stoichiometric flame type presented a central flame front with higher local equivalence ratios. For the lean flame type, a recirculation zone at the flame neck was found to be the main agent in stabilizing IDF with very low global equivalence ratios.

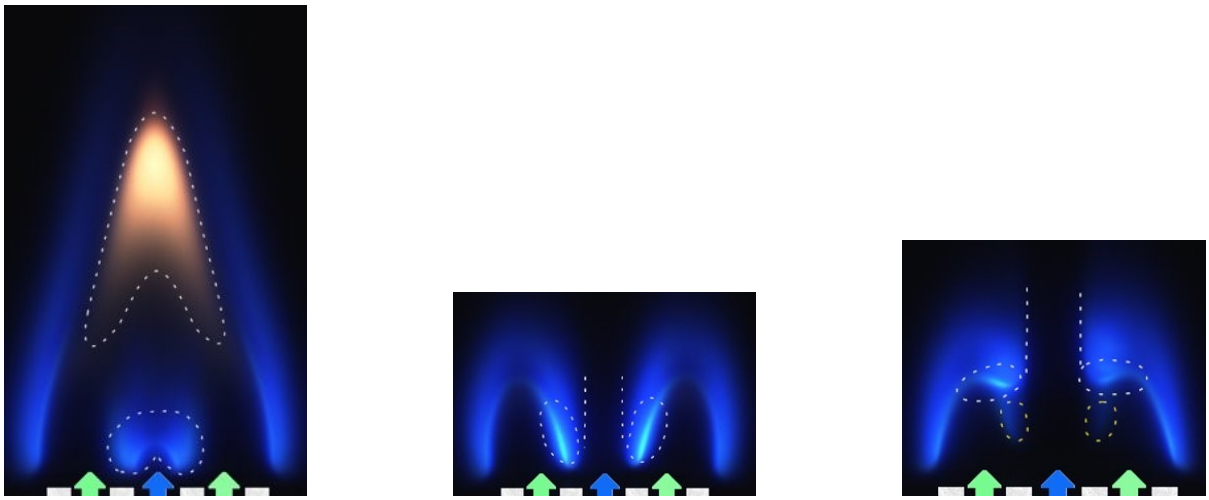

(a) Rich configuration.

(b) Stoichiometric configuration.

(c) Lean configuration.

Figure 1.4: Flame types studied by Ribeiro et al. Source: [34].

1.2.2 Combustion of Hydrogen Enriched Fuels

Most studies regarding combustion of hydrogen enriched fuels are either related to NDFs or premixed flames. Zhang et al. [35] proved that hydrogen improves stability of premixed methane-air flames. Kumar and Mishra [36] reported reduced laminar diffusion flame lengths with hydrogen addition to LPG fuel. Wu et al. [37] also observed that flame length reduces when hydrogen is added to methane. Hu et al. [38] showed that laminar burning velocity of lean methane-air premixed flames increases with H_2 under elevated temperatures and pressures. More recent studies also depict an increase in laminar burning velocity of premixed flames with H_2 addition [39, 40]. In particular, Reyes et al. [18] reported increased burning speed of premixed flames burning methane-hydrogen blends, in parallel with an increase of radiation emitted by CH^* and OH^*, when hydrogen is added to the fuel blend.

In terms of the impact of hydrogen proportion in the fuel blend, on the emission behavior of diffusion and premixed flames, studies point to soot reduction when hydrogen is added to ethylene-air jet diffusion flames [41, 42]. Burbano et al. [43] depicted a significant decrease in the CO emissions for natural gas combustion with hydrogen addition. The same trend of CO emissions was reported for combustion engines burning hydrocarbons enriched with H_2 [44]. In terms of NO_x emissions, [36] reported possible reduced NO_x emissions in a laminar jet diffusion flame, due to reduced residence times through H_2 addition, in spite of increased temperatures with the latter. Han et al. [45] made an interesting study showing

that methane-air, hydrogen enriched, premixed flames exhibit lower NO_x emissions than methane-air, hydrogen enriched, diffusion flames in the same operating conditions.

The only comprehensive study in literature of IDF burning an hydrogen enriched fuel is achieved by Miao et al. [8, 46–48], burning LPG-H_2 fuel in a CAP burner. These studies report a significant increase in the flame stability range with small H_2%. IDF with 50%H_2 and with 0%H_2 seem to have the same structural changes as the global equivalence ratio varies [46]. Further studies by Miao et al. [8] examine three flame stable-related limits and mention that LPG-H_2 IDF can hold stable with lower energy consumption than LPG IDF. Through planar laser-induced fluorescence (PLIF), OH^* is analyzed inside the flame, showing significant combustion enhancements with hydrogen addition. In terms of the impact of H_2 addition on the emission behavior of IDF, depending on the portion of H_2 on the fuel, it may increase or decrease CO and HC emissions, whereas NO_x emissions may reduce with H_2 addition, for lean conditions. In general, very low global equivalence ratios are associated with high CO and HC emissions. NO_x variations with the variation of the global equivalence ratio exhibit different trends according to the range of global equivalence ratios, possibly due to different mechanisms behind the formation of NO_x (Fenimore and Zeldovich) [48].

1.3 Objectives

This work studies the impact of hydrogen addition to methane fuel in an inverse diffusion flame under fuel-lean conditions. It is intended to characterize the flame structure, flow mechanisms and emission behavior using a multi-slit rectangular burner and keeping a constant power supplied to the flame. As mentioned in the previous section, the only study found in literature related to hydrogen combustion through an IDF, until the date this thesis was written, features variable power supplied to the flame and uses a CAP burner - which originates a completely different flame morphology compared to the multi-slit rectangular burner [7, 34]. Furthermore, there is also lack of information regarding flow velocity fields of IDF with hydrogen enriched fuels.
The present work features two main goals:

1. Influence of the H_2 fuel proportion on flame morphology. Namely, it is intended to understand if new flame morphologies are created through hydrogen addition. Furthermore it is important to find if hydrogen alters flame structure within the flame structures already present without hydrogen [34]. A velocity vector map of the flame flow is analyzed, in order to understand the mechanisms triggering flame structure changes through hydrogen addition.

2. Influence of the H_2 fuel proportion on the emission characteristics of the flame. Emissions of CO, CO_2, unburned hydrocarbons (UHC) and NO_x are extensively analyzed within a wide range of global equivalence ratios and three hydrogen percentages. The emissions' results are cross-correlated with the flame structure's results so to investigate if the emission behavior of the flame is correlated with its morphology.

1.4 Thesis Outline

This thesis encompasses four chapters. Chapter 1 provides an overview of some key important parameters of the energy and hydrogen industries nowadays and how hydrogen enriched IDF may build in the modern energy industry. It follows the state of the art, examining the main topics addressed regarding IDF and combustion of hydrogen enriched fuels. Finally, the main objectives of this thesis are stated. Chapter 2 extensively describes the experimental conditions, setups, procedures and techniques. The methods used for data processing are explained and an uncertainty analysis is made. Results of the experiments performed are presented in Chapter 3. Namely, flame structure is first analyzed through flame photography, followed by a velocity analysis of the flame flow field and, finally, emissions from the flame range studied are presented and discussed. To end this work, Chapter 4 summarizes the highlights of this work and provides some guidelines for future work based on this thesis.

Chapter 2

Experimental Analysis

This work is based on three main experiments: flame photography, flow velocity analysis and analysis of the flue gas and temperature of the flames. The experimental setup, for all of the experiments made, comprises a burning system and an acquisition system. The burning system involves the interconnection of the equipment and materials that control the combustion of the fuel mixtures tested. The acquisition system incorporates all the materials and equipment involved in the process of collecting the data of each experiment. For each experiment, the burning system is the same but the acquisition system is different. Furthermore, the experimental techniques and procedures and the data handling of each experiment are completely different. Therefore, this chapter starts by the description of the burning system, which is common for the three experiments. Then, each of the three experiments is described in the correspondent section. Namely, the experimental setups of the acquisition systems, the procedures and techniques and the data handling of each case are reported. Finally, an uncertainty analysis is presented.

2.1 Burning System and Conditions

2.1.1 Burning System

Figure 2.1 schematically represents the burning system. To be sure of the hydrogen and methane proportions on the fuel, and of the fuel flow rate arriving at each fuel channel of the burner, there are four flow meters for the fuel blend. Two for methane and two for hydrogen. Hydrogen and methane are drawn from the research gas bottles (provided by Air Liquid: Alphagaz^{TM} model, with a purity higher than 99.95% (v/v)). Each flow splits in two and enters the flow meter. One of the hydrogen flows then mixes with one of the methane flows in a mixing chamber and the same happens for the other two flows. After mixing, each of the two fuel flows is then conducted into the lateral channels of the burner. Atmospheric air is fed to the flow meter by a compressing line, after passing through a filtering and drying process. It is then directly conducted to the central channel of the burner.

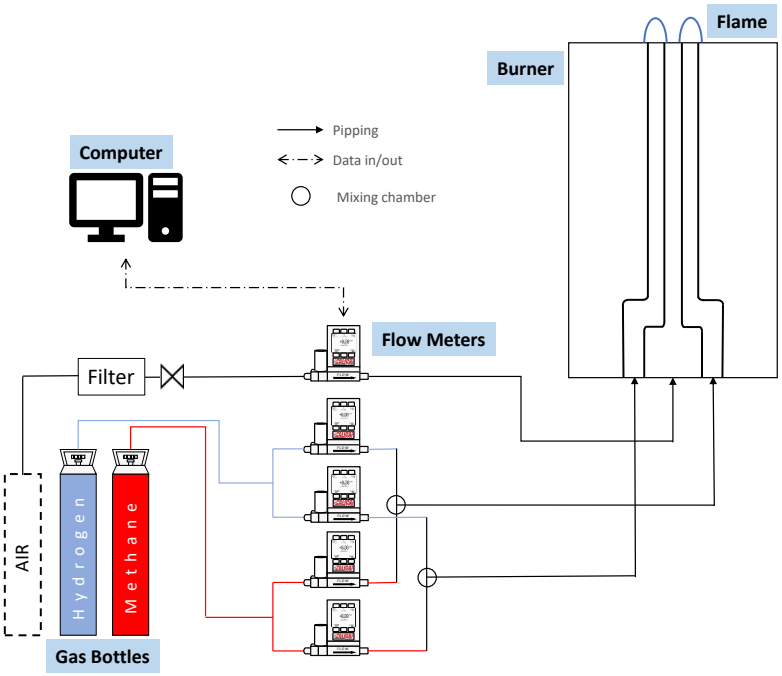

Figure 2.1: Scheme of the burning system.

Burner

The burner used is a two dimensional burner with three rectangular slits at the top, where the flame is anchored, as illustrated in Figure 2.4. Figures 2.2 and 2.3 show the technical drawing of the burner. The burner comprises four 1 mm thick plates, made with AISI 304 Stainless Steel and with a "step like" configuration to ensure a proper flow development and a stable flame at the top. Burner's height is 350 mm and the four slits' length and width at the outlet are 38 mm and 2 mm, respectively. The injection chambers' height and width are 56 mm and 19 mm respectively.

Figure 2.5 presents a close view of the burner's injection chambers. All the interior curvatures were smoothed through the addition of small neoprene fillets. By reducing the formation of corner re-circulation bubbles and pulsating effects on the flame, this assures that the flow keeps laminar throughout the entire length of the plates and that it results in a stable flame.

The 2D flow velocity profile between two parallel plates will only reach a fully developed state when the two boundary layers merge, i.e., when boundary layer thickness equals half of the distance between the plates. Recalling the slit dimensions of $w = 2mm$ and $l = 38mm$, since $l >> w$, it is reasonable to assume the flow is a two-dimensional flow between two parallel plates at a distance w from each other. For such case, the necessary length to achieve a fully developed flow, L_{ent}, is given by [49]:

$$L_{ent} = \frac{Re_w}{5} w \tag{2.1}$$

where,

$$Re_w = \frac{\overline{U} w}{\nu} \tag{2.2}$$

with $\overline{U}$ being the average flow velocity, and ν the kinematic viscosity. The entry length, L_{ent}, was

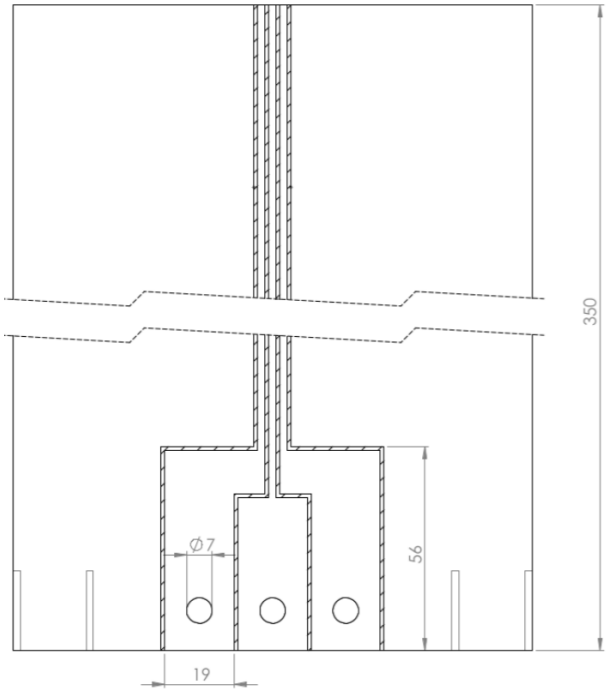

Figure 2.2: Burner technical drawing - cut side view (dimensions in mm).

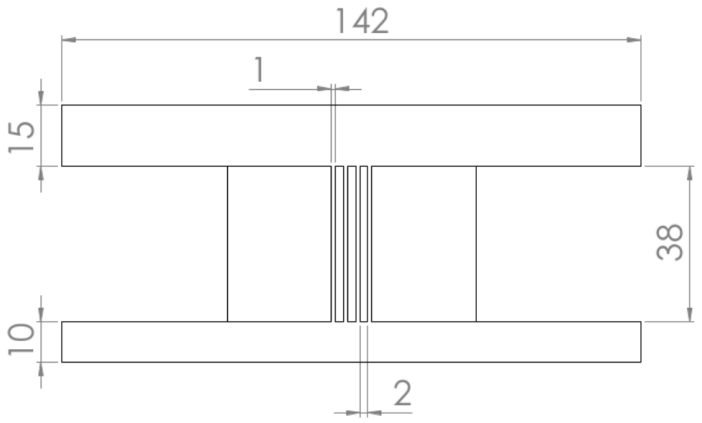

Figure 2.3: Burner technical drawing - top view (dimensions in mm).

calculated for the velocity range under analysis - the length of the plates after the injection chamber, which is 294 mm, was found to be more than enough to ensure fully developed flow at the top of the burner. Theoretically, the flow vertical velocity profile at the exit of each slit should parabolic, given by:

$$U = U_{max}\left(1 - \frac{4x^2}{w^2}\right) \tag{2.3}$$

with the maximum velocity given by,

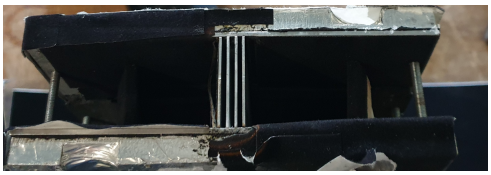

Figure 2.4: 2D burner with three rectangular slits.

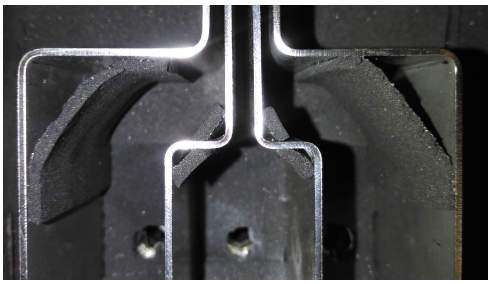

Figure 2.5: Injection chamber fillets.

$$U_{max} = \frac{3}{2}\overline{U} \tag{2.4}$$

where x is the transversal coordinate (perpendicular to the plates). This parabolic flow is represented in Figure 2.6, for an average velocity of, for example, 0.8 m/s, which is a representative velocity of the flows hereby studied.

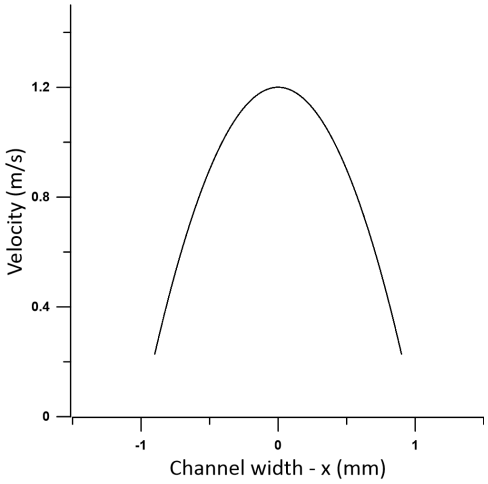

Figure 2.6: Theoretical vertical velocity profile of the flow at the exit of the slit with $\overline{U}$=0.8 m/s and w=2 mm.

Flow Controllers

To control the hydrogen percentage on the fuel blend and the equivalence ratio, five high precision flow meters (Alicat Scientific, MC series) were used. The maximum capacities of the flow meters are 50 SLPM, 5 SLPM (two of the flowmeters) and 1 SLPM (the remaining two flowmeters). Since air presented the highest flow rates, followed by methane and then hydrogen, the 50 SLPM, 5 SLPM and 1 SLPM flow controllers were assigned to air, CH_4 and H_2, respectively. Factory calibration has an average error equivalent to 0.8% of the flow measured over 0.2% of its full scale. Controllers were operated using the LabView^{TM} software.

2.1.2 Burning Conditions

Before describing the burning conditions, an important remark must be made. Being a diffusion flame, the local equivalence ratio of an IDF is, in principle, variable along the flame. Based on most of IDF's studies in literature [6–8, 26, 27, 31, 46–48, 50], a global equivalence ratio, dictated by the relative amounts of fuel and air supplied to the flame, will be used throughout this text (Equation 2.7). To avoid unnecessary misunderstandings, throughout this document, when the symbol "ϕ" or the term "equivalence ratio" are used, they concern to the global equivalence ratio. Conversely, if the local equivalence ratio is to be mentioned, the text will explicitly remark that the mentioned equivalence ratio is a local one, and not the global.

This work focuses on achieving a stable and efficient IDF under ultra-lean conditions, through hydrogen addition to a methane based fuel. Therefore, the range of equivalent ratios hereby studied is predominantly lean. Following the work of Ribeiro et al. [34], and to properly discriminate the effect of hydrogen from other affecting variables, the hydrogen's volumetric percentage on the fuel mixture was varied, keeping a constant power supplied to the flame - 236 W. To effectively assess the hydrogen's fuel proportion effect on the flame, the volumetric percentages of H_2 tested were 0%, 25% and 50% [8, 46–48]. The power supplied to the flame is given by:

$$P = \rho_{\mathrm{CH_4}} \dot{Q}_{\mathrm{CH_4}} \cdot LHV_{\mathrm{CH_4}} + \rho_{\mathrm{H_2}} \dot{Q}_{\mathrm{H_2}} \cdot LHV_{\mathrm{H_2}} \tag{2.5}$$

where ρ is the density, $\dot{Q}$ is the volumetric flow rate and LHV is the the lower heating value of the corespondent fuel component. For a certain power, the values of $\dot{Q}_{\mathrm{CH_4}}$ and $\dot{Q}_{\mathrm{H_2}}$ are found by defining the hydrogen's volumetric proportion on the fuel.

$$x_{\mathrm{H_2}}(volume) = \frac{\dot{Q}_{\mathrm{H_2}}}{\dot{Q}_{\mathrm{H_2}} + \dot{Q}_{\mathrm{CH_4}}} \tag{2.6}$$

For each $x_{\mathrm{H_2}}$, Equation 2.6 is substituted on Equation 2.5 and the values of $\dot{Q}_{\mathrm{CH_4}}$ and $\dot{Q}_{\mathrm{H_2}}$ are obtained. Since, for each H_2% ($= x_{\mathrm{H_2}} \times 100$), $\dot{Q}_{\mathrm{fuel}}$ ($\dot{Q}_{\mathrm{fuel}} = \dot{Q}_{\mathrm{CH_4}} + \dot{Q}_{\mathrm{H_2}}$) is constant, the equivalence ratio is varied by changing the volumetric flow rate of the central air jet, $\dot{Q}_{\mathrm{air}}$. Therefore, one must find an equation relating the equivalence ratio with $\dot{Q}_{\mathrm{air}}$.

$$\phi = \frac{\left(\frac{\dot{Q}_{air}}{\dot{Q}_{fuel}}\right)_{st}}{\left(\frac{\dot{Q}_{air}}{\dot{Q}_{fuel}}\right)} \tag{2.7}$$

where the subscript *st* stands for stoichiometric. As already mentioned, $\dot{Q}_{\mathrm{fuel}}$ is obtained from the H_2% and flame power. The chemical equation for the combustion of a fuel blend, with $x_{\mathrm{H_2}}$ volumetric proportion of H_2, under stoichiometric conditions, is:

$$\begin{aligned} &(x_{\mathrm{H_2}}\,\mathrm{H_2} + (1\text{-}x_{\mathrm{H_2}})\,\mathrm{CH_4}) + (2 - \frac{3\,x_{\mathrm{H_2}}}{2})(\mathrm{O_2} + 3.76\,\mathrm{N_2}) \\ &\longrightarrow (1\text{-}x_{\mathrm{H_2}})\mathrm{CO_2} + (2\text{-}x_{\mathrm{H_2}})\mathrm{H_2O} + (7.52{-}5.64\,x_{\mathrm{H_2}})\mathrm{N_2} \end{aligned} \tag{2.8}$$

Therefore, $\left(\frac{\dot{Q}_{air}}{\dot{Q}_{fuel}}\right)_{st} = \left(2 - \frac{3x_{\mathrm{H_2}}}{2}\right)$ and $\dot{Q}_{\mathrm{air}}$ can now be computed, for each ϕ, through Equation 2.7.

Another important variable throughout this work is the velocity ratio, V_r, between the central air jet and the adjacent fuel jets. Figure 2.7 schematically illustrates the velocities of the three jets in each slit.

$$V_r = \frac{V_{air}}{V_{fuel}}, V_{fuel} = \frac{(\frac{\dot{Q}_{fuel}}{2})}{A_{slit}}, V_{air} = \frac{\dot{Q}_{air}}{A_{slit}} \tag{2.9}$$

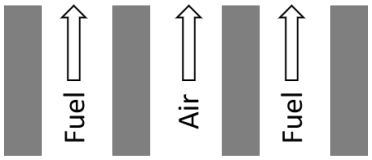

Figure 2.7: Scheme of the velocities of the three jets in each slit.

Finally, the Reynolds number, specially the Reynolds number of the central air jet Re_{air}, has a significant role on the analysis of the IDF hereby studied:

$$Re_{air} = \frac{\rho_{air} V_{air} D_h}{\mu_{air}} \tag{2.10}$$

where μ_{air} is the air viscosity, ρ_{air} is the air density and D_h is the hydraulic diameter of the cross section of the air jet flow, calculated based on [51].

The values of the properties used to compute Equations 2.5 to 2.10 are summarized in Table 2.1.

Table 2.1: Properties of the reacting gases at STP (0^{o}C, 1 bar) - [5, 51].

Properties	Gases		
	Methane	Hydrogen	Air
Density [kg/m^3]	0.708	0.089	1.292
Viscosity [Pa.s]	103	84.3	173
Molecular weight [kg/kmol]	16.04	2.02	28.96
Lower Heating Value [MJ/kg]	50.02	120.0	-

The experimental conditions for 0%H_2, 25%H_2 and 50%H_2 are presented in Tables 2.2, 2.3 and 2.4, respectively.

SLPM stands for standard liters per minute (0^{o}C, 1 bar).

2.2 Flame Photography

Figures 2.8 and 2.9 illustrate the experimental setup used for flame photography. The acquisition system for flame photography involves a camera, lens and a computer. The burner was in a fixed position, aligned with the camera. The whole setup was covered with black panels to prevent disturbances due to possible exterior light penetrations.

The camera used was a JAI CV-M9-GE, 3-CCD RGB with a resolution of 1074x768 pixels. This camera, through a complex prism, separates the incoming light into three beams, which are then filtered to produce three wavelength ranges: blue, red and green. Each of the three CCDs receives one of the three wavelength ranges. This feature provides photos with very accurate color characteristics per pixel,

Table 2.2: Experimental conditions for 0%H_2: $Q_{CH_4} = 0.40$ SLPM, $Q_{H_2} = 0.00$ slpm.

ϕ	Q_{air} (SLPM)	V_r	Re_{air}
0.2	19.0	95.2	1187
0.3	12.7	63.5	792
0.4	9.5	47.6	594
0.5	7.6	38.1	475
0.6	6.3	31.7	396
0.7	5.4	27.2	339
0.8	4.8	23.8	297
0.9	4.2	21.2	264
1.0	3.8	19.0	237
1.1	3.4	17.3	216
1.2	3.2	15.9	198

Table 2.3: Experimental conditions for 25%H_2: $Q_{CH_4} = 0.36$ SLPM, $Q_{H_2} = 0.12$ slpm.

ϕ	Q_{air} (SLPM)	V_r	Re_{air}
0.2	18.7	77.3	1169
0.3	12.5	51.5	779
0.4	9.4	38.6	585
0.5	7.5	30.9	468
0.6	6.2	25.8	390
0.7	5.4	22.1	334
0.8	4.7	19.3	292
0.9	4.2	17.2	260
1.0	3.7	15.5	234
1.1	3.4	14.1	213
1.2	3.1	12.9	195

Table 2.4: Experimental conditions for 50%H_2: $Q_{CH_4} = 0.31$ SLPM, $Q_{H_2} = 0.31$ slpm.

ϕ	Q_{air} (SLPM)	V_r	Re_{air}
0.2	18.3	59.4	1141
0.3	12.2	39.6	761
0.4	9.1	29.7	570
0.5	7.3	23.8	456
0.6	6.1	19.8	380
0.7	5.2	17.0	326
0.8	4.6	14.8	285
0.9	4.1	13.2	254
1.0	3.7	11.9	228
1.1	3.3	10.8	207
1.2	3.0	9.9	190

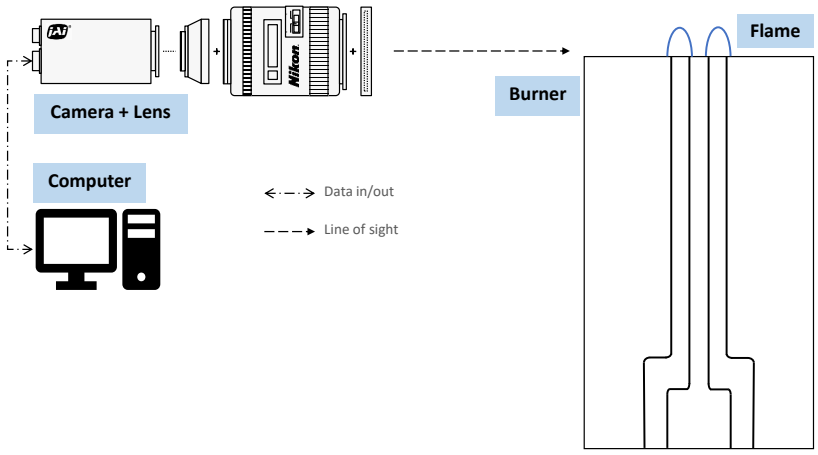

Figure 2.8: Scheme of the experimental setup for flame photography.

especially in low light conditions. The lens used were the Nikon AF NIKKOR 50mm f/1.4D lens. Images were acquired in RAW format, with null gain values. Lens aperture was set to its maximum, f/1.4, and minimum focus distance. Distance and alignment from the camera to the burner were kept constant for all burning conditions. Figures 2.10 (a) and (b) illustrate the camera and lens used, respectively.

2.3 Particle Image Velocimetry

Particle Image Velocimetry (PIV) is a quantitative velocity measuring technique. Its precision and non-intrusive nature make it more attractive than the traditional flow measurement techniques, such as the Doppler velocimetry and hot-wire anemometry. There are no probes disturbing the flow, allowing for

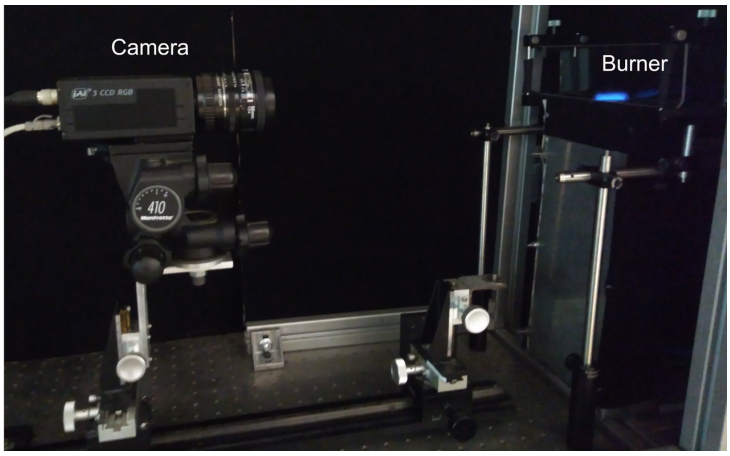

Figure 2.9: Experimental setup for flame photography.

(a) JAI CV-M9-GE, 3-CCD RGB.

(b) Nikon AF NIKKOR 50mm f/1.4D.

Figure 2.10: 3 CCD camera and optical lens.

velocity measurements over the whole field. [52, 53].

This technique uses small tracer particles (alumina in this case) immersed in the flow under study. These particles that travel with the flow will then be illuminated by a double pulse laser in the area under study. The laser produces a planar sheet of green light, with a 532 nm wavelength. The laser is synchronized with a high speed camera, through a synchronizer connected to the central acquisition system. This camera will acquire two frames of the particles illuminated by the laser, such that each frame is taken at the exact moment in which the particles are illuminated by the laser pulse. Having two consecutive frames of the same illuminated particles and the time between the two laser pulses, allows for the determination of velocity. Through a proper calibration, in which pixels distance is converted to millimeters, the supporting software calculates the velocity, dividing the distance traveled by each particle between the two frames by the time between the two laser pulses (Δt). The final result is a 2D velocity field of the area under study.

2.3.1 Setup and Procedure

Figure 2.11 schematically illustrates the experimental setup for the PIV analysis. Figures 2.12 (a) and (b) show a more detailed view of the camera-laser-burner arrangement and the seeding system, respectively. The setup encompasses a camera, lens, filter, laser, synchronizer, computer, tracer particles, two magnetic stirring plates and rods and three bottles containing the particles. The particles are stirred through a magnetic rod which, in turn, is agitated by the electromagnetic stirrer. The flow of fuel/air passes through the correspondent bottle and drags the particles. In order to achieve a reasonable amount of particles immersed in each flow, two magnetic stirrers were used, one for air and another for the fuel flows. This particles travel with the flow all the way up to the flame and are then lit by the laser and photographed by the camera. To protect the CCD sensors of the camera and to obtain proper definition of the particle light scattering, a 532 nm optical filter was used.

The camera used was the HiSense Zyla sCMOS, with a 40 fps frame rate and a resolution of 2560x2160 pixels. Attached to the camera was a Nikon AF NIKKOR 60 mm f/1.28D lens. The laser utilized was a Dantec Dual Power 65-15 Yag, with two laser cavities, each with a maximum laser pulse frequency of 15 Hz and a wavelength of 532 nm. The synchronizer of these two devices was a BNC 575 Series Pulse Generator, controlled centrally by an acquisition system on a dedicated computer, through the software Dantec Dynamic Studio 5.1. The particles used were the Logitech 5 micron Calcinated Aluminium Oxide Powder that did not interfere with the flow. These particles were agitated by two magnetic stirrers, a Velp Scientifica ARE Aluminum Hot Plate Stirrer and a Roth MH 15 magnetic stirrer. Finally, the used filter was a Meller Griot 532 nm.

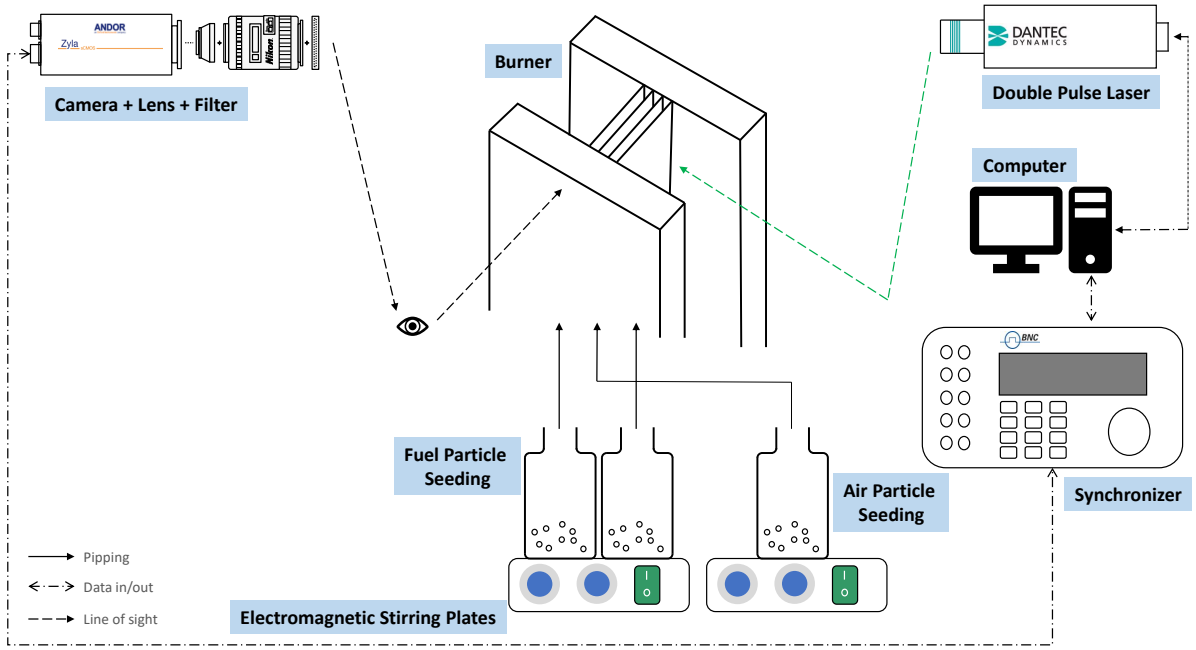

Figure 2.11: Scheme of the PIV experimental setup.

To achieve accurate velocity results, the flow seeding system must be carefully handled. In particular, particle density should be close to that of the flow, to avoid errors related to gravitational effects and

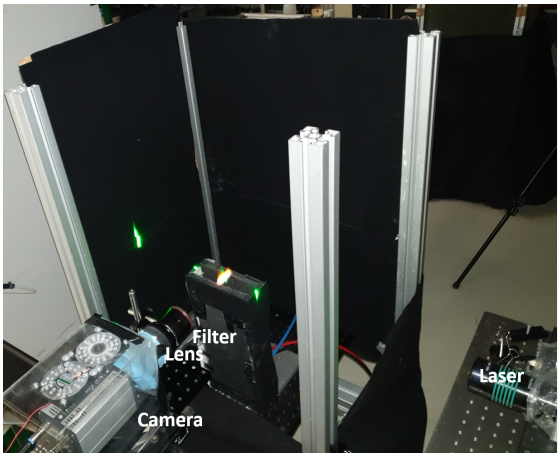

(a) PIV setup: camera-laser-burner arrangement.

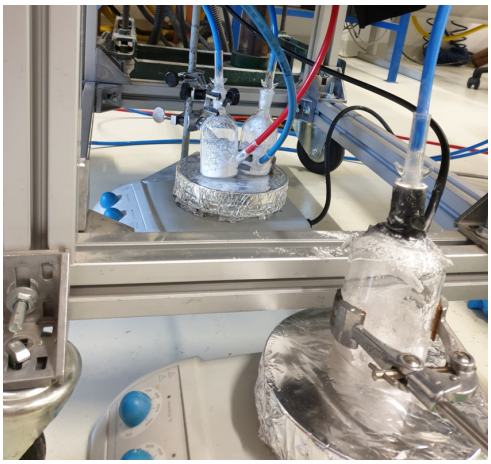

(b) PIV setup: seeding system.

Figure 2.12: Photo of the experimental setup - PIV.

to prevent disturbances in the path of the main flow [54]. Particles must also have good light scattering properties, hence, they cannot be to small [55]. They should be non-corrosive, non-volatile, non-abrasive and non-toxic. [54] suggests the use of particles with 3 μm for gaseous flows. The particles used, of aluminum oxide powder, matched all these requisites, thus being an appropriate choice. Another important concern is the density of particles in the flow, i.e., the amount of particles per unit volume. [56] provided reference to what should be an appropriate density of particles in the flow and appropriate lightning conditions - Figure 2.13.

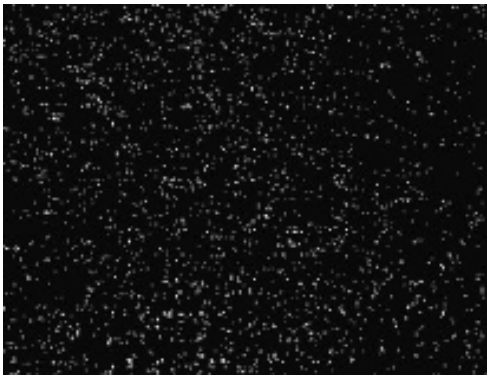

Figure 2.13: Appropriate particle density and illumination reference. Source: [56].

After ensuring that a reasonable amount of particles were immersed in the flow, it was important to adjust the power emitted by the laser and the focus distance. These two adjustments were made together through a trial and error procedure, until an image with well focused particles and good light conditions (enough light to illuminate the particles but not to much, to prevent high saturation levels that could damage the CCD of the camera), such as the one represented in Figure 2.13, was obtained. Finally, calibration was made by photographing a piece of paper with a known distance and converting the pixels distance, in the photo, to the real distance, in millimeters.

2.3.2 Data Processing

Appropriate data processing of the frames acquired by the camera is crucial in obtaining accurate PIV results. After the acquisition, a correlation between each pair of images acquired, to calculate the 2D velocity field has to be employed. Before applying a specific correlation, there are several possibilities in terms of image editing. In this case, no filter was applied. Only image masking was used to limit the area to be correlated.

To calculate the velocity, the software needs two variables: the displacement of the particle and the time interval between the two frames. The latter is set by the user at the time of the acquisition. It corresponds to the time between the two laser pulses. The calculation of the displacement is more complex. The software will divide each image into smaller rectangular areas, called interrogation areas (IA), as represented in Figure 2.14. For each IA of the first frame, the correlation approach will measure the similarity of that IA with the correspondent IA of the second frame. The result will be maximum (peak) for locations where there is more correspondence (pixel by pixel). In other words, the correspondent interrogation areas from each frame, are cross-correlated with each other, pixel by pixel. The correlation produces a signal peak, identifying the common particle displacement - the position of the peak corresponds to the average displacement of the particles in that IA [54, 57]. It is important to remark that, since the displacement calculated on each IA is an average of the displacement of each particle in that IA, it is assumed that the displacements calculated, and thus the velocities, are constant for every particle, over each IA. One velocity vector is generated per IA. Figure 2.15 schematically illustrates the cross correlation method. This correlation approach is called cross correlation and is the main principle behind PIV velocity calculations. Depending on the characteristics of each PIV experiment (type of flow, seeding system, etc), some variants of the cross correlation can be applied.

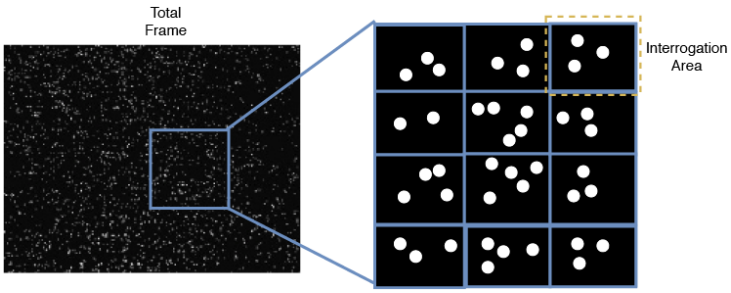

Figure 2.14: Division of each frame into smaller rectangular interrogation areas.

In the case of this experiment, the average correlation was used. In this correlation approach, the cross correlation function of each IA is averaged at each location for all the images. It will increase the signal to noise ratio and generate a clear correlation peak. To obtain accurate velocity values, this correlation approach needs a sufficient number of images so that the total sum of particles in each region is acceptable [56]. Average correlation should be used in cases where it is difficult to keep a constant and reasonable amount of particles flowing during the whole acquisition time. In this experiment, it was difficult to keep a reasonable flow rate of particles during the whole acquisition time, in the fuel slits,

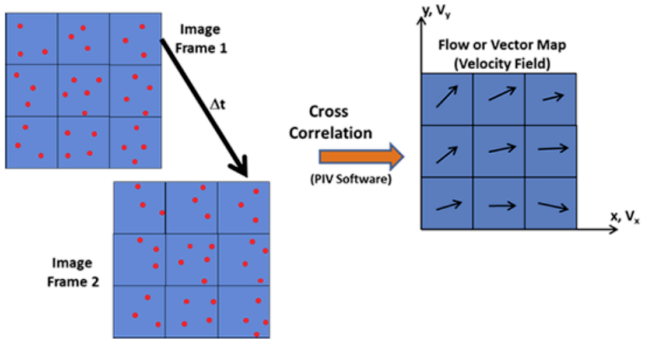

Figure 2.15: Scheme of the cross correlation method to obtain a velocity vector in each IA.

but a lot of image pairs where acquired (two hundred of image pairs per acquisition), therefore, average correlation was a suitable correlation approach for this case.

To apply a specific correlation, one must choose the IA for the analysis and the time between pulses, Δt. As already mentioned, the Δt is set upon the acquisition. If the IA is to small and/or the Δt is to high, a particle that was in a specific IA in the first frame may end up in a different one in the next frame, which leads to wrong velocity values. On the other hand, if the IA is to big, the resolution may not be enough to accomplish a decent study of the flow velocity field, and if the Δt is to small, it may not be enough to allow for a minimum traceable displacement of the particles. In general, the best options involve higher resolutions, i.e., lower IAs. To achieve this, higher velocities will require a lower Δt and vice-versa.

In the present study, only $\phi = 1$ and $\phi = 0.3$ were analyzed. $\phi = 1$ is associated to lower air velocities, so a $\Delta t = 200\mu s$ was used. Conversely, $\phi = 0.3$ is associated to higher air velocities, therefore, a $\Delta t = 60\mu s$ was required to achieve a reasonable resolution. The IA size used was constant: 16 px (horizontal) x 32 px (vertical). Vertical velocity components were much higher than horizontal, hence, vertical dimension of the IA is bigger than the horizontal. Notice that the highest possible resolution in the Dynamic Studio software is 16 px x 16 px. Finally, even with appropriate choices of IA and Δt, some particles may escape from its original IA between the two frames. Therefore, a parameter - overlapping factor - to avoid loss of information must be defined. The overlapping factor will overlap adjacent IA so that particles near the border of the IA in the first frame aren't lost in the second frame [58]. A value of 50% x 50% for this parameter was enough to obtain decent results. Table 2.5 summarizes the PIV parameters used.

Table 2.5: Summary of PIV parameters.

Image pairs per acquisition	200
IA size (px)	16x32
Time between pulses	60 μs and 200 μs
Correlation	Average Correlation
Overlapping factor	50% x 50%

2.4 Flue Gas and Temperature Analysis

This section regards to the study of flame temperature and species concentration of the flue gas emitted by the flame. Namely, emissions from unburned hydrocarbons (UHC), CO, CO_2 and NO_x were analyzed. The experiments concerning the flue gas species concentration were conducted in the Combustion Laboratory of IDMEC.

2.4.1 Setup and Procedure

This section starts by a general overview of the acquisition system. Afterwards, some important details about the setup and procedure are pointed out. Figure 2.16 schematically illustrates the experimental setup of the acquisition system for the analysis of the flue gas species concentration. The system starts by collecting the flue gas sample with an L-shaped probe, placed inside the hood's opening. The sampling gases are cooled as they travel within the probe. Afterwards, the sample passes through a condenser, a silica dryer and a cotton filter - moisture, particles and other condensates are removed. This circuit assures that a clean and dry sample will enter the gas analyzers so that they can properly present the concentration values in an Orsat (dry) reference basis. After the cotton filter, the sample passes through the pump and then through the flow meter, ensuring that the probe aspirates a constant flow of flue gas, that is adequate to enter the analyzers. Finally, the sample passes through the analyzers. All pipping connections are made of polytetrafluoroethylene (Teflon), which is chemically inert, preventing the sample from being contaminated. The analyzers send an electric analogue signal to an acquisition board - Data Translator DT 9802 12 bit - which converts it to digital, at a sampling frequency of 100 Hz. The acquisition board is connected via USB to a computer, which runs the software HP VEE-LAB v5.02 to collect the data regarding the gas species concentration. The sampling period is 30 seconds for each measurement.

Hood

In order reduce the amount of atmospheric air aspirated by the probe and to reduce heat losses by the flue gas to ambient air, a hood was placed on top of the burner. Figure 2.17 shows a photo of the hood-burner connection. The hood consists of a hollow quartz cylinder with 50 cm length, external diameter of 4.5 cm and internal diameter of 3.3 cm. As Figure 2.17 shows, the hood was fitted in a rounded slot with a diameter equal to the external diameter of the cylinder. Hence, the fit of the cylinder within the rounded slot was tight and without openings. Nevertheless, the connection between the cylinder and the slot was sealed with aluminum tape[1] to make sure there was no air entrainment. The rounded slot was attached to the top of the burner with a strong adhesive tape, so that a steady and stable connection was obtained. In order to further prevent possible air admissions into the interior of the hood, this connection was also completely sealed with multiple layers of aluminum tape. Finally, the top of the hood was also partially covered with the same tape, to reduce the ambient air entrainment into the hood and, eventually, into the probe. However, this cover was only "partial" since this flame, as it will be explained in the next chapter,

[1] Aluminum tape was used so that the seal could withstand high temperatures

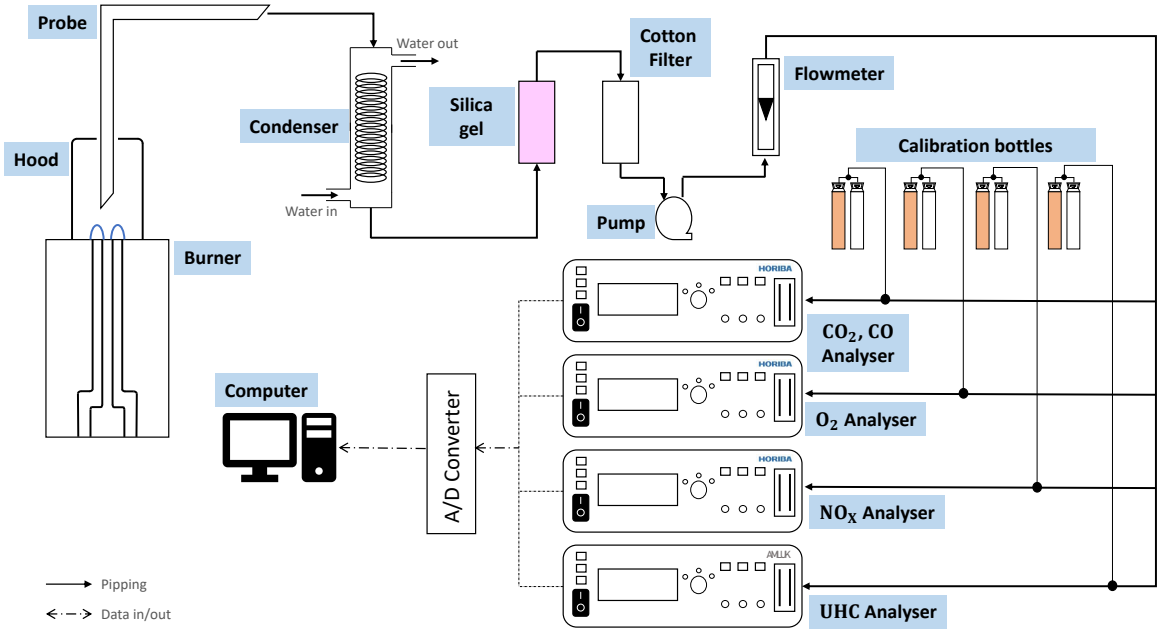

Figure 2.16: Scheme of the experimental setup for the flue gas analysis.

needs not only the center air jet to burn the fuel jets, but also some ambient air. Without ambient air, the flame would not hold stable. Therefore, a small opening around the probe, enough to keep the flame stable, was present.

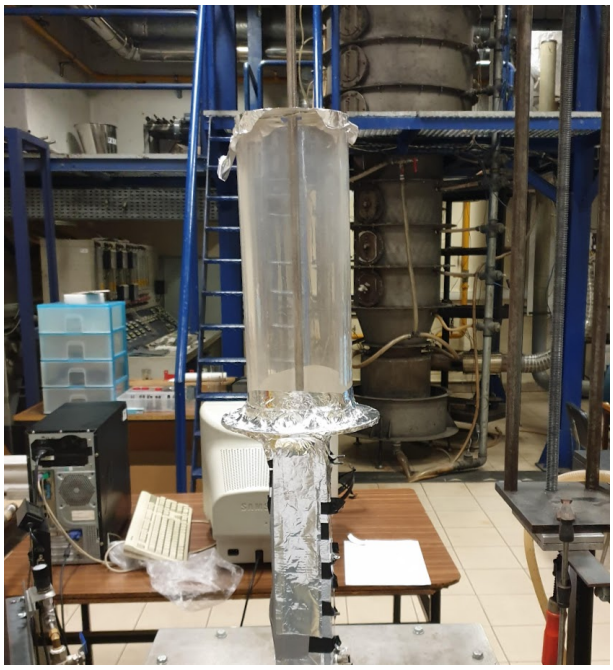

Figure 2.17: Experimental setup for the flue gas analysis: connection between the hood and burner.

Suction Probe

Figure 2.18 presents a schematic illustration of the suction probe used to collect the sample of released gas by the flame. The probe has a hollow L-shape. It is made of stainless steel and its dimensions are shown in Figure 2.18. This device has two channels: an inner channel, through which the sample flows, and an outer channel, through which water flows. The water flow inside the probe is for refrigeration, blocking any further temperature dependent chemical reactions and preventing it from melting, when subject to high temperatures. The vertical portion of the probe was aligned with the center of the central rectangular slit. Its tip was at a vertical distance of about 5 cm from the burner's top. This distance fulfills a commitment between not being too close to the flame and not being too far from it. If the probe is too close, it may overheat, reactions may still be ongoing at the place where the sample is being collected and/or stability of the flame may be compromised. If the probe is too far from the flame, an exaggerated amount of atmospheric air may be aspirated by the probe, thus introducing a high degree of dilution into the sample. The probe is supported on a screw-driven vertical linear slide for vertical positioning, with an uncertainty of 0.5 mm. The gases not aspirated by the species probe are collected by the laboratory exhaust. The flue gases are directly sent to the latter, if the species probe is not being used.

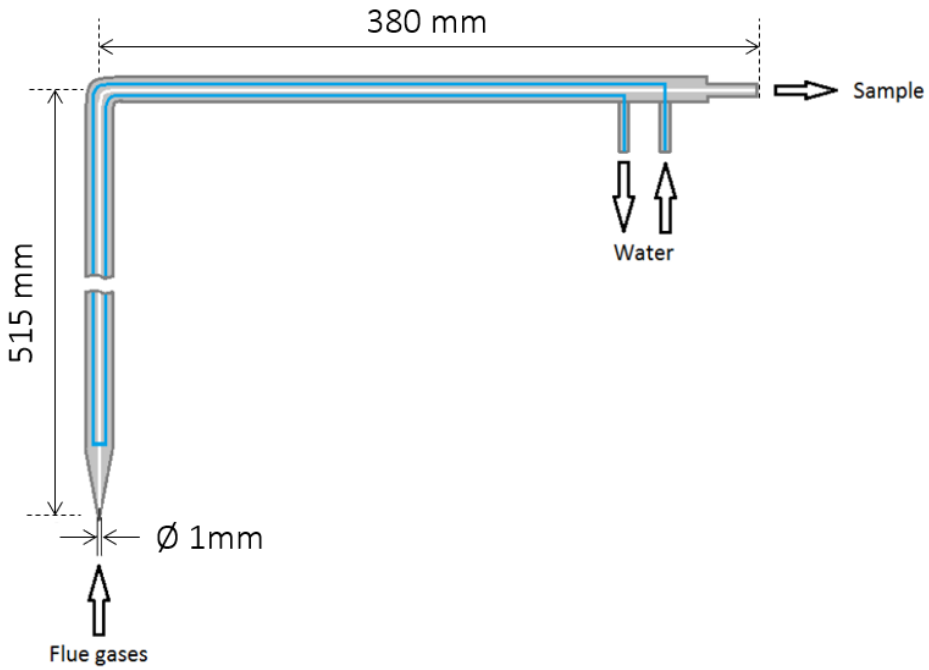

Figure 2.18: Scheme of the probe used to collect the flue gas sample.

Gas Analyzers

The gas analyzers have different characteristics depending on gas species being analyzed. Table 2.6 summarizes the information regarding the gas analyzers used.

Table 2.6: Specifications of the gas analyzers.

Gas Species	Brand - Model	Analysis Method	Measuring Range
CO	Horiba - CMA-331 A	Nondispersive infrared	0 - 5000 ppm (vol.)
CO_2	Horiba - CMA-331 A	Nondispersive infrared	0 - 50% (vol.)
NO_x	Horiba - PG-250	Chemiluminescence	0 - 50 ppm (vol.)
UHC	Amluk - FID 2020 E	Flame ionization detection	0 - 1000/10000 ppm (vol.)

Temperature

The experimental setup for the temperature measurements is shown in Figure 2.19. Temperature measurements were made in the same conditions as of the flue gas measurements. The burner-hood connection is equal to the one shown in Figure 2.17. The top of the hood was also partially covered with aluminum tape. A thermocouple was placed at a vertical distance from the top of the burner of 5 cm and its vertical body was also aligned with the center of the central rectangular slit. The difference between these two setups relies on the acquisition system.

Temperatures were measured through a simple thermocouple, shown in Figure 2.20. The working principle of this device is based on two different metals alloys that are fused together, at a specific point called "hot junction". Depending on the temperature to which the hot junction is subject, a certain voltage is generated. The thermocouple used is type R (Pt/Pt-13%Rh) - it has a platinum anode and a cathode made from a platinum alloy, with 13% rhodium. These two wires are isolated within a ceramic tube (that withstands high temperatures) and they have no point of contact with each other (besides the hot junction). The diameter of the hot junction is 65 μm. This device is rated for temperatures up to 1900 K, which is enough for the temperature range analyzed since no values near or above this limit were observed. After passing through the ceramic tube, the wires are connected to an acquisition board - Data Translation DT9828 - which amplifies and filters the signal. This analogue signal is converted to digital at a rate of 100 Hz. The board communicates with a computer via software - QuickDAQ 2013. The sample period for each measurement was also 30 seconds.

2.4.2 Data Processing

As it was mentioned in the previous section, the top of the hood was not completely covered, since this flame needs ambient air to stabilize. Hence, a dilution effect of the surrounding air, aspirated by the probe, thus diluting the sample, should be carefully concerned. Turns [5] refers to emission indices and corrected concentrations as being the most frequently used forms of expressing emission levels. Both of these forms erase the influence of dilution effects by ambient air. Indeed, for the case of IDF's studies involving emission characteristics of the respective flames [26, 30, 31, 33, 48, 59], emission indices seem to be the most reported form of expressing emission levels. Therefore, to properly confront the emissions of the flames herein studied with those of the most prominent references of similar studies with this one, an approach based on emission indices was opted.

The emission index for species i is the ratio of the mass of species i emitted to the mass of fuel burned

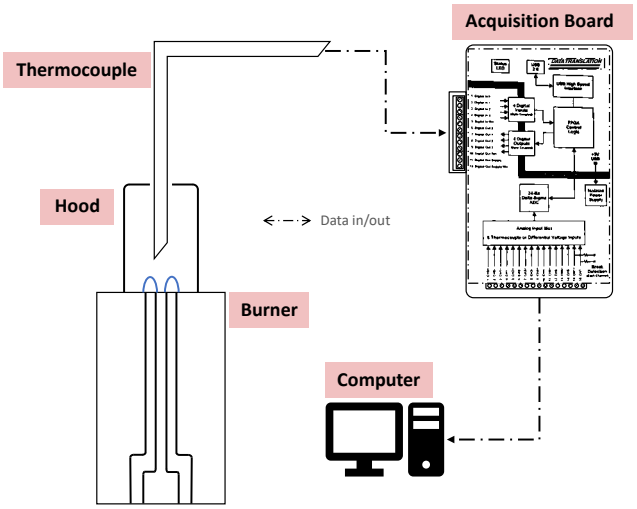

Figure 2.19: Scheme of the experimental setup to measure temperatures.

Figure 2.20: Thermocouple type R with a 65 μm diameter.

by the combustion process [5]:

$$EI_i = \frac{m_{i,emitted}}{m_{f,burned}} \tag{2.11}$$

Assuming that all of the carbon fuel appears in the combustion products in the form of CO, CO_2 and UHC, the emission index of species i is given by:

$$EI_i = \left(\frac{\chi_i}{\chi_{CO_2} + \chi_{CO} + \chi_{UHC}}\right)\left(\frac{xMW_i}{MW_f}\right) \tag{2.12}$$

where the χs are the volumetric fractions of the species analyzed (measured by the gas analyzers), x is the number of moles of carbon in a carbon fuel C_xH_y, and MW_i and MW_f are the molecular weights of the species i and the fuel, respectively. This is the traditional method for calculation of emission indices of hydrocarbon fuels. The measured concentration of i is normalized with all the carbon-contained emissions and the result is used to calculate how many kilograms of species i are emitted per 1 kg of fuel burned. The ratio $x/\left(\chi_{CO_2} + \chi_{CO} + \chi_{UHC}\right)$ accounts for the dilution effect and, when multiplied by the diluted concentration of species i, χ_i, eliminates the dilution effect.

In this study, the fuel blend contains not only hydrocarbon fuel but also hydrogen fuel. Since hydrogen

contains no carbon, one may predict a reduction in carbon emissions per kg of fuel burned when hydrogen is added to the fuel. However, hydrogen's density is much lower than that of methane, its lower heating value is much higher [5], and the power supplied to the flame does not change when hydrogen is introduced in the fuel blend. From these three propositions, results the fact that the mass flow rate of fuel supplied to the flame will decrease with H_2 addition. Therefore, the traditional calculation of the emission indices, Equations 2.11 and 2.12, is not going to express unambiguously the hydrogen's effect on the emission characteristics of the flame. For example, the introduction of H_2 in the fuel blend, keeping the power constant, is expected to reduce CO_2 emissions - as power is constant, a portion of methane fuel is going to be replaced by hydrogen, and the carbon content of the fuel reduces, thus carbon content of the emissions, including CO_2, should also be reduced. However, since the denominator in the formula of the emission index, Equation 2.11, is the mass of fuel burned, and this one is decreasing with the increase of H_2%, the trend of the emission indices obtained for CO_2 is not going to reproduce clearly the evolution of CO_2 concentration in the gas mixture released by the flame.

To overcome this constraint, Turns [5] suggests another frequently used expression, which is also based on the emission index:

$$\frac{Mass\,of\,species\,i}{Fuel\,energy\,supplied} = \frac{EI_i}{\Delta h_c} \tag{2.13}$$

where Δh_c is the heat of combustion of the fuel. Using this equation, emissions are reported in mass of species i emitted per amount of fuel energy supplied to the flame. Therefore, with constant power supplied to the flame, the effect of H_2 addition to the fuel blend on the emissions analyzed, mainly the carbon related emissions, can now be assessed through a clear trend of the gas species concentration on the flue gas, expressed in the units of kg (or g) of species emitted per MJ of burned fuel.

To calculate the emissions through Equation 2.13, the emission indices and the heat of combustion of the fuel must be calculated. The latter is given by:

$$\Delta h_c = \frac{\rho_{\mathrm{CH_4}}\dot{Q}_{\mathrm{CH_4}}}{\rho_{\mathrm{CH_4}}\dot{Q}_{\mathrm{CH_4}} + \rho_{\mathrm{H_2}}\dot{Q}_{\mathrm{H_2}}} LHV_{\mathrm{CH_4}} + \frac{\rho_{\mathrm{H_2}}\dot{Q}_{\mathrm{H_2}}}{\rho_{\mathrm{CH_4}}\dot{Q}_{\mathrm{CH_4}} + \rho_{\mathrm{H_2}}\dot{Q}_{\mathrm{H_2}}} LHV_{\mathrm{H_2}} \tag{2.14}$$

Regarding the fuel blend as 1 kmol of C_xH_y, the values of x and y can be obtained through the following equation:

$$\begin{cases} x = \left(1 - x_{\mathrm{H_2}}\right) \\ y = 4\left(1 - x_{\mathrm{H_2}}\right) + 2x_{\mathrm{H_2}} \end{cases} \tag{2.15}$$

The molecular weight of the fuel blend is given by:

$$MW_f = \left(1 - x_{\mathrm{H_2}}\right) MW_{\mathrm{CH_4}} + x_{\mathrm{H_2}} MW_{H2} \tag{2.16}$$

Combining Equations 2.14, 2.15 and 2.16 with the values obtained by the gas analyzers for $\chi_{\mathrm{CO_2}}$, χ_{CO}, χ_{UHC} and χ_i, and with the value of MW_i, emissions can be obtained in the form of mass of species emitted per fuel energy supplied to the flame. Table 2.7 summarizes the fuel constants used to calculate the emission indices and the heat of combustion of the fuel.

Table 2.7: Summary of the fuel constants used to calculate the emissions.

$\%H_2$	x	y	MW_f (kg/kmol)	Δh_c (kJ/kg)
0	1	4	16	50000
25	0.75	3.5	12.5	52830.7
50	0.5	3	9	57800.6

2.5 Uncertainty Analysis

2.5.1 Uncertainty of the Flow Controllers

To assess the uncertainty induced by the flow controllers, the total uncertainty, for a given flow rate in a flow controller, is given by:

$$U_{\dot{Q}} = \pm \left(0.008\dot{Q}_m + 0.002\dot{Q}_{max}\right) \tag{2.17}$$

where $U_{\dot{Q}}$ is the uncertainty of the flow rate $\dot{Q}$, $\dot{Q}_{max}$ is the maximum allowed flow rate of the flow controller and $\dot{Q}_m$ is the measured flow rate. Knowing the uncertainties associated to each flow meter and which flow meter was used for each gas, it is possible to compute the error associated with the flow meters, $e_{\dot{Q}}$. Table 2.8 summarizes the uncertainties and errors obtained for the maximum and minimum values of air flow rate, for the three fuel compositions studied.

Table 2.8: Uncertainties and relative errors of the flow controllers for extreme conditions.

$\%H_2$	Condition	Gas	Q_m (SLPM)	Q_{max} (SLPM)	U_Q (SLPM)	e_Q
$0\%H_2$	Maximum	CH_4	0.2	5	± 0.0116	5.800%
		H_2	0	-	-	-
		Air	12.69	50	± 0.20152	1.588%
	Minimum	CH_4	0.2	5	± 0.0116	5.800%
		H_2	0	-	-	-
		Air	3.17	50	± 0.12536	3.955%
$25\%H_2$	Maximum	CH_4	0.182	5	± 0.011456	6.295%
		H_2	0.061	1	± 0.002488	4.079%
		Air	18.75	50	± 0.25	1.333%
	Minimum	CH_4	0.182	5	± 0.011456	6.295%
		H_2	0.061	1	± 0.002488	4.079%
		Air	3.12	50	± 0.12496	4.005%
$50\%H_2$	Maximum	CH_4	0.154	5	± 0.011232	7.294%
		H_2	0.154	1	± 0.003232	2.099%
		Air	18.29	50	± 0.24632	1.347%
	Minimum	CH_4	0.154	5	± 0.011232	7.294%
		H_2	0.154	1	± 0.003232	2.099%
		Air	3.05	50	± 0.1244	4.079%

The uncertainties presented have a downstream influence on the hydrogen's volumetric percentage and on the equivalence ratio ϕ. This influence is estimated by means of an error propagation method [60].

Volumetric hydrogen fraction on the fuel

The H_2 volumetric fraction of each mixture was computed using Equation 2.6. Using the error propagation formula,

$$U_{x_{\mathrm{H_2}}} = \pm \frac{\dot{Q}_{\mathrm{H_2}}}{\dot{Q}_{\mathrm{H_2}} + \dot{Q}_{\mathrm{CH_4}}} \sqrt{\left(\frac{U_{\dot{Q}_{\mathrm{H_2}}}}{\dot{Q}_{\mathrm{H_2}}}\right)^2 + \left(\frac{\sqrt{U^2_{\dot{Q}_{\mathrm{H_2}}} + U^2_{\dot{Q}_{\mathrm{CH_4}}}}}{\dot{Q}_{\mathrm{CH_4}} + \dot{Q}_{\mathrm{H_2}}}\right)^2} \tag{2.18}$$

where $U_{x_{\mathrm{H_2}}}$ is the uncertainty associated with the volumetric proportion of H_2. Using the results obtained for $U_{\dot{Q}_{\mathrm{H_2}}}$ and $U_{\dot{Q}_{\mathrm{CH_4}}}$, the maximum values of $U_{x_{\mathrm{H_2}}}$ can be calculated. Table 2.9 summarizes the results.

Table 2.9: Maximum uncertainties and relative errors of the volumetric fraction of H_2 for 25%H_2 and 50%H_2.

%H_2	$U_{x_{\mathrm{H_2}}}$	$e_{x_{\mathrm{H_2}}}$ (%)
25	± 0.0159	6.36
50	± 0.0218	4.37

Equivalence ratio

As already stated, the equivalence ratio is given by Equation 2.7. Equation 2.7 can be manipulated to obtain:

$$\phi = \frac{a\dot{Q}_{fuel}}{y^{air}_{\mathrm{O_2}}\dot{Q}_{air}} \tag{2.19}$$

where $y^{air}_{\mathrm{O_2}}$ is the average molar fraction of oxygen in the atmosphere at sea level - here assumed to be 0.2095 [61] - and a is the stoichiometric coefficient of oxygen for complete fuel combustion. Recall that, from Equation 2.8, a depends on the hydrogen's volumetric fraction on the fuel mixture, $x_{\mathrm{H_2}}$:

$$a = 2 - \frac{3x_{\mathrm{H_2}}}{2} \tag{2.20}$$

Neglecting the uncertainty related to the fluid's density, the uncertainty of ϕ can be estimated using the following equation:

$$U_\phi = \pm \frac{\left(2 - \frac{3x_{\mathrm{H_2}}}{2}\right)}{0.2095\dot{Q}_{air}} \sqrt{U^2_{\dot{Q}_{\mathrm{fuel}}} + \left(\frac{\dot{Q}_{\mathrm{fuel}}}{\dot{Q}_{\mathrm{air}}}\right)^2 U^2_{\dot{Q}_{\mathrm{air}}}} \tag{2.21}$$

where U_ϕ is the uncertainty of the equivalence ratio. Using the uncertainties calculated for the flow meters in the correspondent section, it is straightforward to estimate U_ϕ and e_ϕ. The results of the maximum uncertainties of the equivalence ratio for the three fuel mixtures are presented in Table 2.10.

Table 2.10: Maximum uncertainties of ϕ for 0%H_2, 25%H_2 and 50%H_2.

%H_2	U_ϕ	e_ϕ (%)
0	± 0.0846	7.05
25	± 0.0842	7.02
50	± 0.0746	6.22

Observing all the errors obtained, it is possible to conclude that the error never exceeds approximately

7%.

2.5.2 PIV Uncertainty Analysis

As mentioned before (section 2.1.1), the flow in each channel can be modeled as being a parabolic flow, given by Equations 2.3 and 2.4. Therefore, this flow can be taken as representative for comparison with the empirical values. The flow hereby analyzed is the flow of air, in the central channel, right at its exit (at the exit of the central slit). The flow analyzed presents an average velocity of 0.8 m/s (correspondent to $\phi = 1$ and $0\%H_2$), which is a representative condition of this work. Figure 2.21 presents the theoretical velocity profile against the empirical values obtained for the vertical velocity component of the flow. Five PIV acquisitions with air flowing in the central channel were made, always in the same conditions. To properly simulate the conditions of the PIV tests to obtain the results further along, 200 pairs of frames were acquired per acquisition, the Δt and the IA size were 200 μs and 16 x 32 px, respectively.

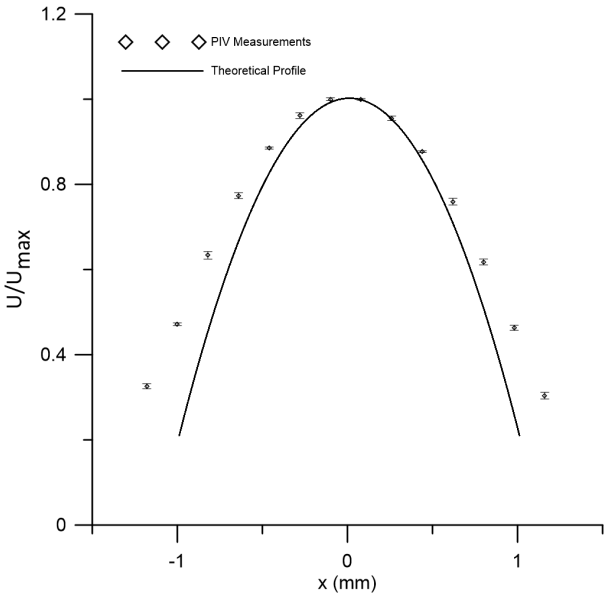

Figure 2.21: PIV Uncertainty - Dimensionless empirical velocity values vs dimensionless theoretical velocity profile.

As Figure 2.21 shows, the error bars are very short, almost imperceptible - the maximum registered velocity fluctuations from the measured average velocity were registered at the borders (near the plates), being about 1.6% of the average velocity measured at that location. Nevertheless, in general, velocity fluctuations were small, showing a reasonable precision of the PIV measurements.

In regards to the theoretical profile, the root mean square, Equation 2.22, of the velocity deviations from the theoretical profile were 0.2 m/s, which represent 16.67% of the theoretical center line velocity. Since the plates that form the channels have a finite length, in contrast to the theoretically infinite plates, more boundary layer effects are expected and thus more velocity deviations from what theory predicts. Also, disturbances caused by burner imperfections and particle seeding inconsistencies may promote higher deviations from the theoretical profile. The highest velocity deviations from the theoretical profile were seen to occur near its center line (center of the channel's width: near U_{max}), having a value of 27% of

the maximum theoretical velocity.

$$RMSE = \sqrt{\frac{\sum_{i=1}^{n}(P_i - O_i)^2}{n}} \tag{2.22}$$

where P_i are the predicted velocities by the theoretical profile, O_i are the observed velocities and n is the number of velocities analyzed.

2.5.3 Flue Gas and Temperature Uncertainty Analysis

Flue Gas

The repeatability uncertainty of the gas analyzers is ± 0.5% of the full scale used for CO_2, NO_x and CO, and ± 1% of the full scale used for UHC. The values obtained for the uncertainties associated to the measurements of each gas species concentration are summarized on Table 2.11. The uncertainties of

Table 2.11: Uncertainties associated with the measures of the gas species concentrations.

Uncertainties	CO	CO_2	NO_x	UHC
$U_{emissions}$	± 25 ppm	± 0.25 %vol.	± 0.25 ppm	± 10/100 ppm

the gas species concentration values propagate to the the emissions measured in grams of emitted species per mega joule of fuel supplied to the flame, since the latter is based on the gas species concentration. Regarding the flame configurations[2] studied herein, the maximum uncertainties associated with these emissions, are presented in Table 2.12. Regardless of the uncertainties just presented, before each session

Table 2.12: Maximum uncertainties of the emissions in the form of (g/MJ).

$\%H_2$	U_{CO} (g/MJ)	U_{CO_2} (g/MJ)	U_{UHC} (g/MJ)	U_{NO_x} (g/MJ)
0	± 0.00313	± 0.492	± 0.007161	± 0.00000336
25	± 0.00472	± 0.742	± 0.0108	± 0.00000506
50	± 0.00527	± 0.827	± 0.012	± 0.00000564

of measurements, the analyzers were calibrated, in order to make sure the reference values are measured correctly, and to ascertain both their accuracy - deviation from reference value - and precision - deviations among measurements. The calibration of NO_x, CO_2 and CO analyzers was performed with a calibration bottle containing 150 ppm of NO, 8 %vol. of CO_2 and 750 ppm of CO, with the rest being nitrogen. The UHC analyzer was calibrated with a calibration bottle containing 80 ppm of CH_4, the rest being N_2. All measurements showed a deviation of less than 4 % of the reference value. To assess the maximum reproducibility uncertainties, measurements were repeated, at least, four times. These ones showed values lower than 8% for CO and CO_2 and lower than 14% for NO_x and UHC.

Temperature

Uncertainties associated with the temperature measurements are the same as of the thermocouple's uncertainty. According to [62], for a thermocouple with a length to diameter ratio greater than 200,

[2] A specific flame configuration is defined by its ϕ and by its volumetric H_2%.

convection and radiation processes play an important role on heat transfer, even more so than conduction. Radiation interferes and alters the temperature measurements, and it is stated that variations of ± 100 K are predictable. Therefore, for this work, the uncertainty of the thermocouple is 100 K.

Chapter 3

Results

Naturally, flame structure and luminosity of an IDF are highly correlated with parameters such as stoichiometry, fuel and air velocities, fuel type and burner geometry [21]. To adequately assess the impact of the fuel's hydrogen content on the flame, in a multi-slit rectangular burner, this section presents the results of a series of experiments performed while keeping a constant power (P = 236 W). Equivalence ratio was varied by changing the air flow rate. Since this work is focused on achieving clean and efficient combustion performances, by using hydrogen, in fuel-lean conditions, the range of equivalence ratios tested was $0.2 \leq \phi \leq 1.2$. It should be noted that, although power kept constant, hydrogen volumetric percentage on the fuel was set at 0%, 25%, 50%. Therefore, for a fixed H_2 percentage, the fuel flow rate is constant for all equivalence ratios, but it varies according to the hydrogen dose on the fuel. Air-fuel velocity ratio, V_r, is thus controlled by the air flow velocity alone.

This chapter comprises three sections - in all of them, the impact of hydrogen percentage on the fuel mixture is studied. First, an analysis of the main flame structures is presented. Then, a study of the velocity fields in two key flame morphologies is conducted. Finally, the emission characteristics of all flame configurations are introduced.

3.1 Flame Structure

Figure 3.1 shows photographs for the complete range of flames studied. Two distinct flame types were identified, Type I and Type II, and their structure is prominent across the whole chapter. Since these flame types have already been described, without hydrogen, by Ribeiro et al. [34], focus will be on the effect of the fuel's H_2% on those morphologies, and only a basic description of these two flame types will be made.

Figures 3.2 (a) and 3.2 (c) illustrate the visual appearance of flames Type I and II, respectively. Flame Type I holds from $\phi = 1$ to $\phi = 0.8$, for 0%H_2. This equivalence ratio range is extended to $\phi = 0.5$, for 25%H_2 and to $\phi = 0.3$, for 50%H_2, whereas flame Type II holds from $\phi = 0.5$ to $\phi = 0.2$ for 0%H_2. From $\phi = 0.4$ to $\phi = 0.2$, for 25%H_2 and, finally, for 50%H_2, it is only present when $\phi = 0.2$. Figure 3.3 schematizes the range of equivalence ratios for each flame type. Flame structures between these two

types, like the one represented in Figure 3.2 (b), are the transition from Type I to Type II and its study is not relevant for this work, since these flames are not stable. However, its photography is left here to help the reader understand the flame type transition mechanism. Flame configuration with $\phi = 0.2$ and $0\%H_2$ did not exhibit stable characteristics also, hence, it is not addressed in this discussion. Finally, flame configurations with $\phi = 1.1$ and $\phi = 1.2$, for all $H_2\%$, which are also Type I flames, are not presented here. Their appearance and structure are just the same as for $\phi = 1$ and correspondent $H_2\%$.

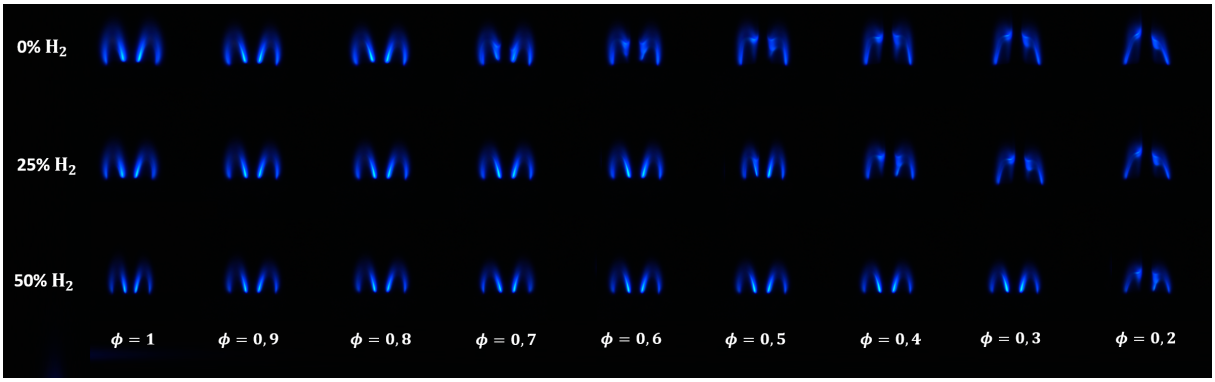

Figure 3.1: Full range of flames studied.

(a) Flame Type I ($\phi = 1$; $V_r = 19$; $0\%H_2$).

(b) Transition Flame ($\phi = 0.6$; $V_r = 32$; $0\%H_2$).

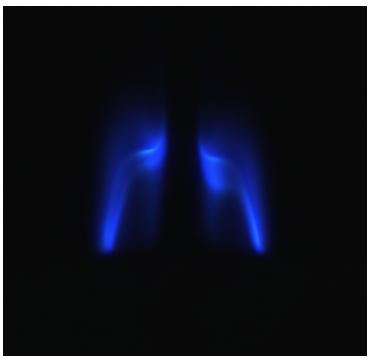

(c) Flame Type II ($\phi = 0.3$; $V_r = 63$; $0\%H_2$).

Figure 3.2: Flame types.

3.1.1 Flame Type I

Flame Type I has an "M" shaped body and features two important flame regions, as indicated in Figure 3.4 (a). Flame Region A (FRA) is the main flame region, in which most of the fuel is entrained by the low pressure, high velocity central air jet. Its intense blue light shows that there is a good mixing of the reactants due to this entrainment effect [6, 31, 46, 50]. The second flame region, Flame Region B (FRB), corresponds to the burning of the fuel particles, that did not follow the air jet, with the adjacent ambient air [34]. Luminosity of FRB is more intense right at the exit of the fuel slits. FRB then stretches and looses luminosity. For the same $H_2\%$, these flames have very similar flame lengths, meaning that flame length is mainly affected by the H_2 proportion on the fuel and not by Re_{air}.

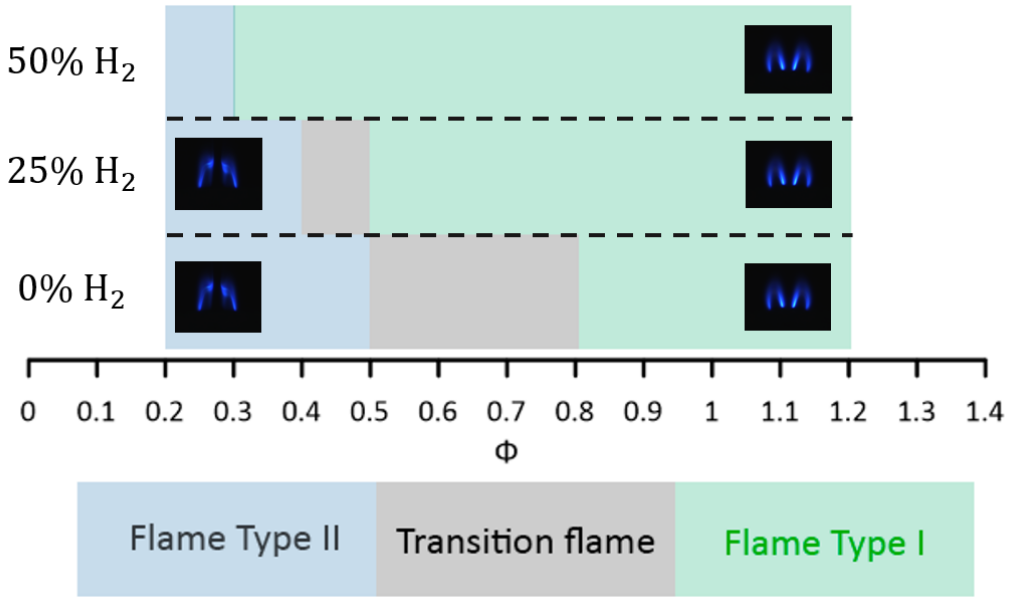

Figure 3.3: Equivalence ratio range for each type of flame, for each H_2%.

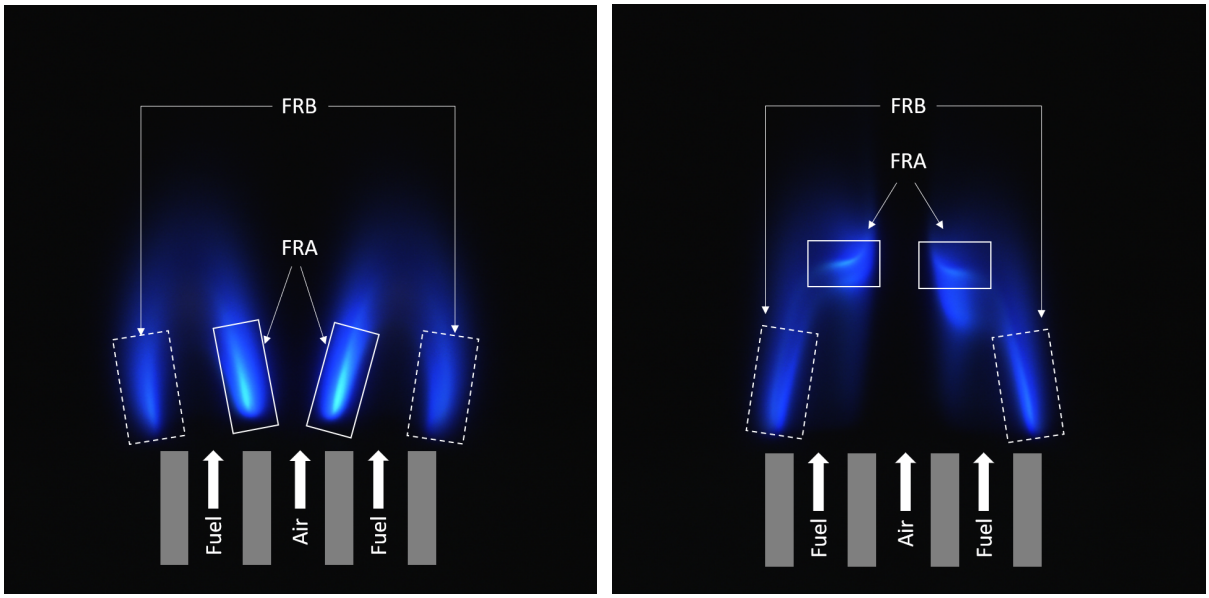

(a) Flame Type I - Flame regions ($\phi = 1$; $V_r = 19$; 0%H_2). (b) Flame Type II - Flame regions ($\phi = 0.3$; $V_r = 63$; 0%H_2).

Figure 3.4: Flame types - description.

3.1.2 Flame Type II

Increasing Re_{air} will increase the V_r and decrease the equivalence ratio, eventually reaching a Type II flame, which has a "neck-like" structure [7, 8, 27, 46]. The mass flow rate of air is so big that it creates a shear lifting force on FRA, shifting its position to a higher one, and making its luminosity and area become notably lower, as illustrated in Figure 3.4 (b). Miao et al. [8] reported three effects associated with escalating Re_{air}, which seem to apply in the present case:

1. Entrainment force on fuel due to negative pressure difference;

2. Shear lifting force acting on FRA;

3. Air jet momentum;

Starting with Flame Type I and increasing Re_{air}, even if 1. promotes better mixing of the reactants and enhances combustion in FRA, effects 2. and 3. will prevail over 1. and flame structure will change to that of Flame Type II. High Re_{air} (and velocity) leads to a shear lifting force, pushing FRA upwards, stabilizing it downstream and reducing its area. The air jet is cold and has high momentum (high mass flow rate). FRA of flame Type II is small and its reaction rate is not enough to preheat and ignite most of the air jet (and its entrained fuel). The luminosity of FRB also dropped slightly because the V_r is now bigger and more fuel is entrained faster by the central jet, leaving less fuel particles to burn with ambient air [7]. These flames are under high strain rates, caused by the high shear lifting forces. As Re_{air} increases, strain rate increases, flame stretches and flame length slightly increases.

3.1.3 Effect of Hydrogen Addition

In terms of flame structure, and regarding the flame range studied hereby, the effect of hydrogen addition is divided in two possibilities:

1. Flame type does not change;

2. Flame type changes;

It should be noted that, for the same equivalence ratio, hydrogen addition will decrease the velocity ratio. Power is kept constant and hydrogen has a heating value much higher than that of methane (more than double), meaning that the fuel mass flow rate needed is much smaller. But, since density (kg/m^3) of hydrogen is almost ten times lower than that of methane [5], the fuel volumetric flow rate will increase with hydrogen percentage, and so will fuel velocity.

Focusing on the case in which flame type does not change, consider, for example, Figure 3.5, which shows the evolution of flame Type I with the hydrogen proportion on the fuel. Hydrogen, with small density and high thermal diffusivity, increases the reaction rate of the mixture [11, 30, 63–65]. Therefore, even if flame structure is the same, stability is improved and flame length and width decrease. The fact that V_r is now smaller, may predict a small stretching of the flame [27], but the effect of hydrogen's high reaction rate prevails and flame length actually decreases. Also, radiation within the visible region of the emission spectrum of the $0\%H_2$ flame tends to diminish with H_2 addition because hydrogen combustion emits ultraviolet radiation, not visible. V_r is smaller (and so is the entrainment effect), meaning that reactants might not be so well mixed as they were before, however, hydrogen is very diffusive and enhances mixing with air, making up for the loss in V_r.

Another point of view worth considering is, for the same flame type and $H_2\%$, varying the equivalence ratio. Figure 3.6 shows the flame Type I range, with $50\%H_2$. Flame length is constant since hydrogen proportion and fuel flow rate are the same for all cases. Interestingly, the blue light of FRA gradually increases its intensity. This may be related with the fact that V_r is increasing, thus promoting a better air-fuel mixing.

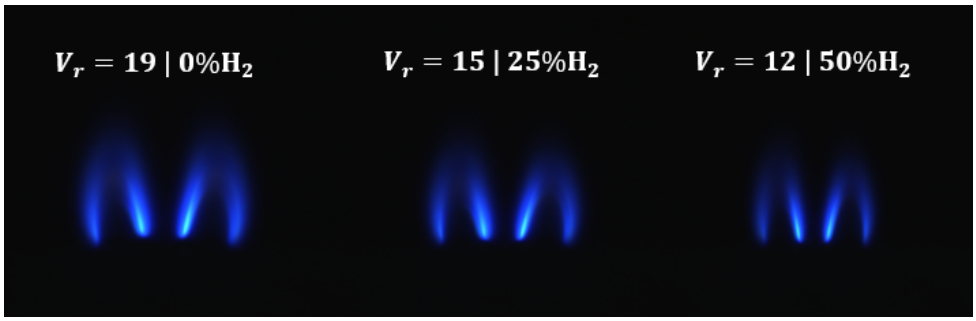

Figure 3.5: Evolution of flame Type I ($\phi = 1$) with H_2 addition on fuel.

Figure 3.6: Flame Type I range with 50%H_2.

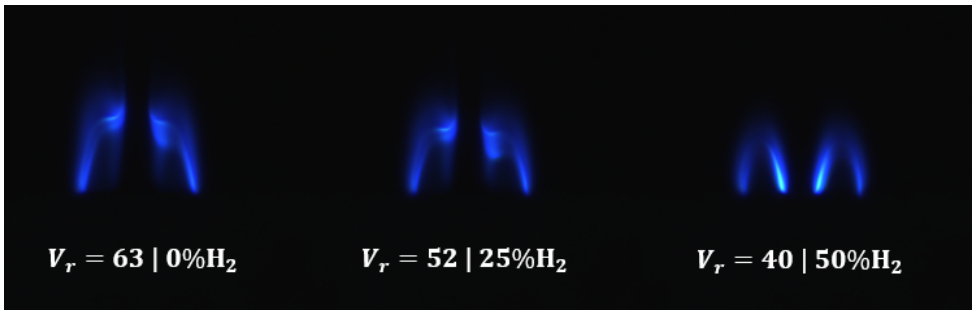

Figure 3.7: Evolution of flame Type II ($\phi = 0.3$) with H_2 addition on fuel.

Going through the case in which flame structure changes, consider, for example, Figure 3.7, which displays the evolution of a Type II flame, starting without hydrogen. Due to its high heat of combustion and high thermal diffusivity, H_2 promotes a higher reaction rate and has lower ignition energy than methane alone. Ignition of reactants is faster, temperature increases and so does reaction rate. The small FRA of flame Type II increases its reaction rate and ignites the high momentum cold air jet and entrained fuel (with lower ignition energy requirements now). FRA increases its area to form flame Type I and anchor the center of the flame in the burner. This rise of FRA's area changes the velocity field of the flame (this will be studied with more detail in section 3.2) and the shear lifting force is not enough to lift FRA [47].

Note that velocity ratio is smaller with H_2. A smaller V_r is typically associated with poor mixing quality of reactants and flame stretch [7]. Despite this situation, the effect of hydrogen's higher diffusivity and higher reaction rate prevails: mixing quality increases and flame length slightly decreases.

3.2 PIV Analysis

This section encompasses the results and its discussion regarding the impact of the fuel's H_2% on the flow characteristics of the flames hereby studied. Ribeiro et al. [34] reported an extensive PIV analysis for flames Type I and Type II without hydrogen, hence, focus will be on the impact of H_2. As explained in section 3.1.3, hydrogen addition may change the flame type or not, depending on its equivalence ratio. Naturally, major changes of the flow velocity fields occur for the case in which flame structure is affected by hydrogen. Therefore, the main subject of this analysis is the discussion of the effects of hydrogen when it converts flame Type II into flame Type I. For the case in which flame type does not change due to H_2 addition (flame Type I), flow velocity fields do not show major differences, neither do the velocity profiles. Consequently, this case is not approached in this text. H_2 has no impact on FRB from flames Type I and II. Furthermore, these flame regions were already extensively studied in [34]. Therefore, FRB from both flames is also not addressed in this section.

3.2.1 Flame Type I vs Flame Type II

Figure 3.8 (a) shows the vector mapping of flame Type II ($\phi = 0.3$, 0%H_2). Since this this flame has the highest velocity ratio ($V_r = 63$), the size of the vectors of the lateral fuel jets is to small when compared to those of the central air jet. Therefore, the small rectangle in Figure 3.8 (a) is expanded in Figure 3.8 (c). As Figure 3.8 (a) illustrates, first, by continuity and due to boundary layer effects, the air jet slightly expands after exiting the central slit. Immediately after the exit of the slits, the fuel jets are entrained by the low pressure central air jet. Subsequently, a narrow section arises, in which air and fuel improve their mixing quality due to high momentum diffusion from the central air jet to the fuel jets. Finally, that narrow section expands when it reaches FRA on the sides. It expands because FRA, being a combustion zone, is hot and releases the hot flue gases that expand and accelerate due to their decreased density [34, 66]. Recalling section 3.1.2, this flame is highly inefficient - along that narrow section just mentioned, the entrained fuel mixes with the central air and, part of it, escapes combustion by passing in between the two FRAs. As expected, the most luminous regions of the flame, FRA, are located in flow regions where velocity gradients are very high, as it can be seen from the change in color of the vectors. The high velocity gradients promote the inter-mixing between air and fuel due to momentum diffusion bringing combustion closer to stoichiometric conditions.

Figure 3.8 (b) illustrates the vector mapping of flame Type I, with the same ϕ, but now with 50%H_2. By increasing the reaction rate, hydrogen will cause the flame to anchor in the burner and reduce its length. As soon as the air jet leaves the burner, it expands and mixes with the fuel entrained. Since now FRA Type I is present, combustion starts right after the exit of the burner and the combustion area is much higher. There is much more fuel being burned, by FRA Type I. Therefore, instead of having the narrow section that was seen in flame Type II, now there is FRA Type I in that zone. The reactants are very hot due to preheating and the flue gases are even hotter. By continuity, the hot, less dense gases will accelerate and expand. As it can been seen in the vector mapping, the flow field from flame Type I is much wider and adhered to the burner in contrast to the narrow and stretched flow field of flame Type

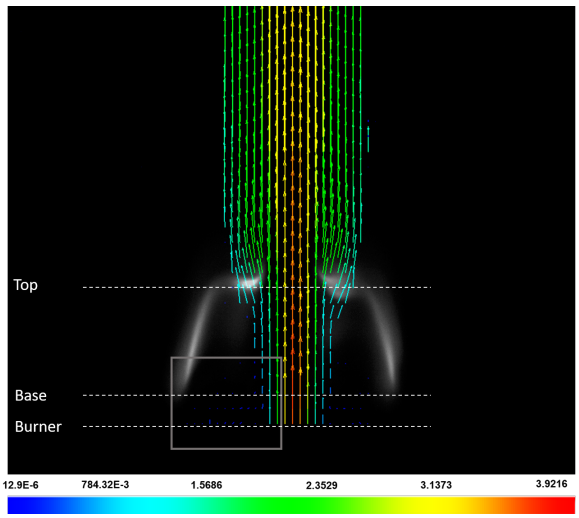

(a) Vector mapping - flame Type II ($\phi = 0.3$, 0%H_2, $\Delta t = 60$ ms, IA=16x32).

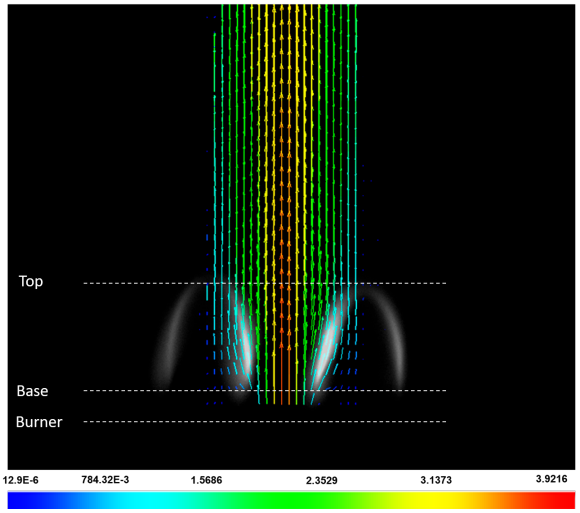

(b) Vector mapping - flame Type I ($\phi = 0.3$, 50%H_2, $\Delta t = 60$ ms, IA=16x32).

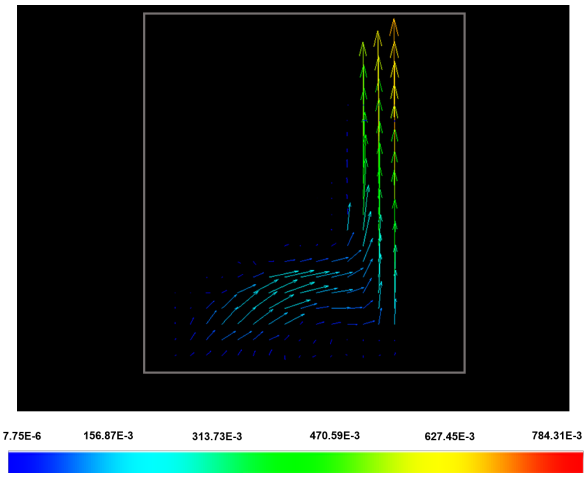

(c) Fuel exit detailed - flame Type II (region highlighted in (a)).

Figure 3.8: Vector mapping of flames Type I and II.

II. The portion of air and entrained fuel that was escaping combustion is now being burned in FRA Type I and contributing to anchor the flow on the burner and to extend it laterally. Although this flame is actually much more efficient than Type II, it should be remarked that there is still a small fraction of the central air jet and, probably, some entrained fuel, that does not take part in the combustion process. Similarly to what was observed in Flame Type II, the most luminous zone of the flame, FRA Type I, is located in a zone where high velocity gradients predominate. High velocity gradients generate high momentum diffusion from the air jet to the fuel jets. Mixing quality of the reactants is improved and combustion occurs closer to stoichiometric conditions, thus, emitting more light.

Figures 3.9 (a) and (b) show the vertical velocity profile of the two flames under consideration at the base and top of them, respectively - positions "base" and "top" are indicated in Figures 3.8 (a) and (b), for flames Type II and I, respectively. The rectangles on the x axis represent the slits that separate air and fuel. At the base of the flame (1 mm from the exit of the burner), velocity profiles are very similar. With 50%H_2, velocity of the central air jet is slightly lower since the air flow rate, for the same ϕ and with

H_2 on the fuel blend, is also slightly lower. Since hydrogen has a density almost ten times smaller than that of methane at room temperature, fuel flow rate of Type I flame is higher at the exit of the burner. Conversely, on the top of both flames, velocity profiles are much more different from each other. Velocity profile of flame Type I presents much higher velocities in the outskirts of the central air jet. As the flow from Flame Type I adheres to the burner and expands laterally, the hotter and less dense combustion products show up with high velocities farthest from the center. On the contrary, as already mentioned, flame Type II presents a narrow velocity field, with higher velocities only showing up closer to the central air jet.

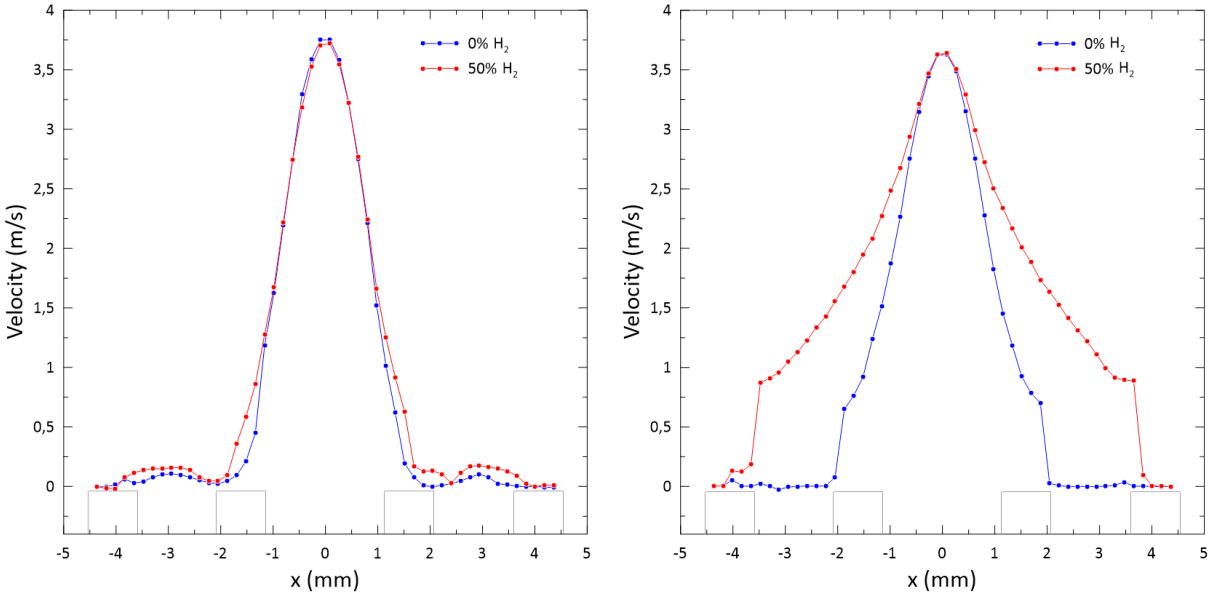

(a) Velocity profile - Base ($\phi = 0.3$, $\Delta t = 60$ ms, IA=16x32). (b) Velocity profile - Top ($\phi = 0.3$, $\Delta t = 60$ ms, IA=16x32).

Figure 3.9: Vertical velocity profiles of flames Type I ($\phi = 0.3$, 50%H_2) and II ($\phi = 0.3$, 0%H_2). The squares represent slits' position at the burner outlet.

3.3 Flue Gas and Temperature Analysis

In this section, results from the experiments to measure the emission characteristics of the range of flames studied are presented and discussed. This analysis is divided in two main subsections, one for CO_2, UHC and CO - evolution of each of these gases is correlated with the other two - and another to NO_x and temperature of the flue gas. In each of these subsections, the general evolution of each species is first analyzed. A study of the emissions for each flame type, addressing the impact of H_2%, is then conducted. The results are all presented in grams of emitted gas per mega joule of fuel supplied. Recalling that this work is focused on fuel-lean conditions, the analysis in this section will, in general, start from stoichiometric conditions (higher equivalence ratios) towards leaner conditions (lower equivalence ratios). Since each discussion will be divided in flame Type I and flame Type II, it is important to recall Figure 3.3 and to consider the range of ϕ for the flame type under study, according to each H_2%.

3.3.1 Emissions of UHC, CO and CO_2

The results for the emissions of UHC, CO and CO_2 are presented in Figures 3.10 (a), (b), and (c), respectively. UHC and CO have very similar evolutions since both of them are associated with incomplete combustion. In general, when ϕ decreases, the UHC and CO emissions increase. Conversely, CO_2 is associated with complete combustion, thus having an opposite trend - when ϕ decreases, its emissions decrease too. Combustion is less efficient for leaner air-fuel mixtures. Miao et al. [48] also verified similar evolutions for UHC, CO and CO_2.

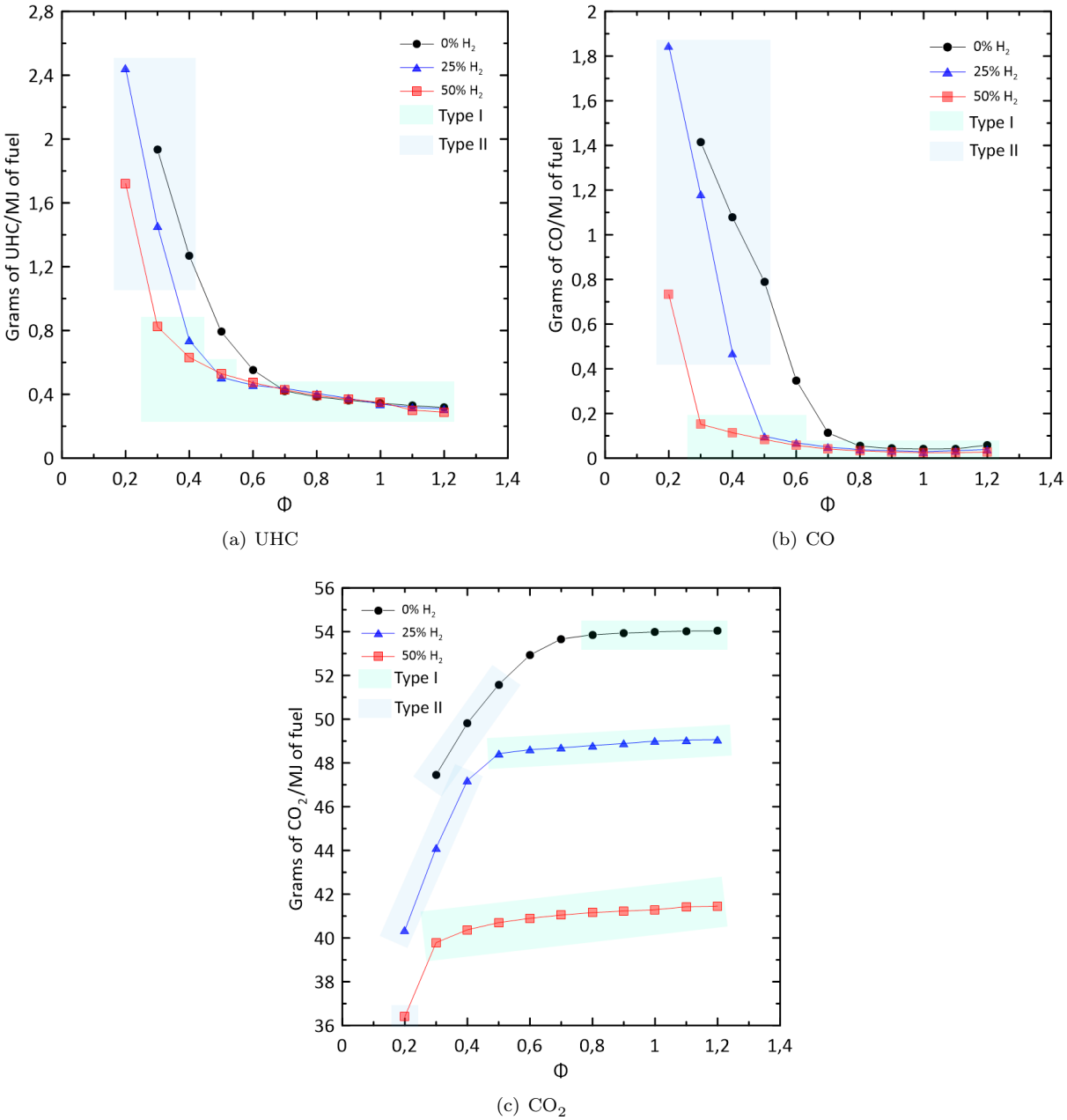

(a) UHC

(b) CO

(c) CO_2

Figure 3.10: Variation of UHC, CO and CO_2 emissions with ϕ for 0%, 25% and 50% of H_2. Highlighted sections of the plots correspond to emissions of flames Type I and II.

Flame Type I

Recalling the analysis of section 3.1, flame Type I equivalence ratio range is extended with hydrogen addition to the fuel mixture. Therefore, the segment of each plot for flame Type I is longer, in the horizontal direction, with increasing H_2%. When Re_{air} increases, velocity of the air jet and entrained fuel also increases. Residence times are lower and there is less time for complete combustion. Combustion starts to be more incomplete and the emissions of CO and UHC slightly increase [26, 31, 48]. In contrast, but for the same reasons, CO_2 slightly decreases as Re_{air} increases.

Comparing the evolutions of UHC and CO, even though they are similar, its values are slightly different and the increase of UHC with Re_{air} is steeper than that of CO. Values of CO are approximately zero for all Type I configurations, meaning that, for flame Type I , combustion is nearly complete. However, if we look at the UHC emissions for the same conditions, they never reach zero. Consequently, there is a (very small) portion of the fuel that does not even participate in combustion. To explain this phenomena, consider, for example, flame Type I with $\phi = 1$ and 50%H_2. This flame emits about 0.35 grams of UHC per MJ of fuel supplied. CO emissions are zero, therefore, combustion must be complete. If combustion is complete for stoichiometric conditions and there are UHC (unburned fuel) as a flue gas, that means there is also some air not participating in combustion, which is in accordance with the observations made within the PIV analysis. A possible reason behind this phenomena may be the fuel entrainment by the central air jet. From the PIV analysis, it was stated that a portion of the central air jet may be not reacting with the lateral fuel jets, even in flame Type I. Some of the entrained fuel into the air jet may be transported or diffused into this non reacting portion of the air jet, thus, precluded from ignition. As equivalence ratio drops and V_r escalates, more UHC are entrained by the air jet and more UHC are emitted. Despite this fact, the portion of unburned fuel is minimal and combustion by flame Type I is, in general, very efficient.

To study the consequences of the fuel mixture's H_2%, consider, again Figures 3.10 (a), (b) and (c). Since the power supplied is constant, the addition of H_2 reduces the carbon content of the fuel. Therefore, carbon related emissions, in general, are also reduced with hydrogen addition. As Figure 3.10 (c) shows, there is a significant and expectable loss in CO_2 emissions as hydrogen's content of the fuel increases. However, analyzing the emissions of UHC and CO from flame Type I, Figures 3.10 (a) and (b) do not show a significant decrease of those gases with H_2%. The values of the emissions of the products of incomplete combustion are stable, for a certain equivalence ratio, for all hydrogen percentages on the fuel mixture. Consequently, the effect of hydrogen on flame Type I does not increase the efficiency of combustion. This means that the efficiency of the combustion process does not depend directly on the H_2% of the fuel but on flame morphology. Miao et al. [48] also found that H_2% does not affect the emissions of CO and UHC for percentages lower than 60%. Note that, for $0.7 \leq \phi \leq 1.2$, hydrogen addition actually decreases CO emissions. That decrease is, however, very small, since emissions were already almost zero without hydrogen. For the case of UHC, as explained before, there is a stable amount of them that will always be emitted from flame Type I, as a result of its structure. Therefore, since hydrogen addition to flame Type I does not change its structure, it will not result in significant variations of UHC emissions.

Flame Type II

Consider now the range of ϕ of flame Type II, according to each H_2%. Observing the three evolutions, as Re_{air} grows, it is clear that there is an equivalence ratio, for each H_2%, triggering a steep increase of both UHC and CO, and a steep decrease of CO_2. Taking a look back at Figures 3.1 and 3.3, this equivalence ratio is, approximately, the same ϕ that marks the transition from flame Type I to Type II. Notice that the steep increase of UHC as flame Type II appears, indicates that there is an escalating amount of fuel that does not even participate in the combustion process, in accordance with the description made in sections 3.1.2 and 3.2.1. As Re_{air} increases, the shear lifting force acting on FRA and the high momentum of the air jet come into play, as mentioned in section 3.1.2. Miao et al. [48] reported three reasons leading to high UHC and CO emissions under fuel-lean condition: quenching effect, high strain rate and insufficient reaction time. The shear lifting force is the agent behind the high strain rate. This high strain rate of FRA stabilizes it on top of the flame and eradicates most of its area. It leads to the extinction of FRA Type I to a new much smaller and less luminous FRA Type II. This extinction phenomena due to high strain rate was also verified by [29]. The quenching effect and insufficient reaction time derive from the high momentum and low temperature of the central air jet. The high velocity of the air jet results in small residence times, which are insufficient to ensure complete combustion. The mass flow rate of air and entrained fuel is very significant and is cold. When the reacting fuel (FRA) impinges on it, the combustion process quenches because reaction rate on FRA is not enough to completely burn the fuel mixture. The combination of these three effects results in a sharp increase of UHC and CO when ϕ decreases. Conversely, but for the same reasons, CO_2 will decrease steeply when ϕ decreases, within the range of flame Type II configurations. Hence validating the argument that combustion efficiency abruptly decays upon reaching flame Type II.

As for the case of flame Type I, for the case of flame Type II, increasing H_2% promotes a decrease of CO_2, UHC and CO emissions, due to reduction of the carbon content of the fuel. As it was explained before, CO_2 decreases because the carbon content of the fuel is reduced with hydrogen addition [48]. Emissions of CO and UHC decrease with H_2% due to flame morphology differences - caused by hydrogen addition. For example, consider Figures 3.11 (a) and (b). While (a) has a structure Type II fully developed, (b) still has a portion of the right side of FRA in transition from Type I to Type II[1]. This portion of FRA that is not yet completely extinguished, is still burning some UHC and CO. There is more fuel under combustion and the reaction rate is higher, thus contributing to the reduction of those gases in the flue gas composition. Also, hydrogen addition to the fuel, for the same ϕ and same power supplied, will slightly decrease the flow rate of the central air jet. Residence times increase and there is more time to burn UHC and CO.

3.3.2 Emissions of NO_x and Temperature

In order to contextualize the NO_x emissions within the temperature evolution, first, a brief analysis of the latter is presented. The NO_x emissions' behavior for flame Type I and II and its dependency of the

[1] This distinction is pointed out here to analyze the emissions of flames Type II but, in general, flame configuration with $\phi = 0.2$ and 50%H_2 is considered to be Type II.

(a) $\phi = 0.2$; 25%H_2 (b) $\phi = 0.2$; 50%H_2

Figure 3.11: Flame Type II.

hydrogen's content of the fuel are then discussed.

As indicated in the description of the experimental setup of the flue gas analysis, temperature of the flue gas was measured in the same place where the probe aspirates the combustion products - about 5 cm from the flame's top. Therefore, the measured temperature is far from being adiabatic. As Figure 3.12 (a) shows, as ϕ increases and Re_{air} decreases, temperature increases since global conditions are brought closer to stoichiometric. In contrast to the variations of the combustion gases with ϕ, temperature variation with ϕ is roughly linear. Meaning that, apparently, it is not much affected by flame morphology, i.e., the flame type. Also, the effect of hydrogen is not significant until $\phi = 0.8$. For higher equivalence ratios (flame Type I, in this case), there is a very tiny decrease in temperature as hydrogen increases. This temperature decrease might by related to the decrease in flame length of flame Type I, as the hydrogen content of the fuel increases. Since flame length decreases, distance to the thermocouple increases and combustion products are more cooled down by the cold ambient air. Nevertheless, the mentioned temperature differences are very small and are within the uncertainty range of the thermocouple's measured values. Therefore, it is not possible to draw more reliable conclusions, with this data.

Figure 3.12 (b) presents the variation of NO_x emissions with the equivalence ratio for 0%, 25% and 50% of hydrogen on the fuel blend. Just like in the case of CO_2, UHC and CO, starting from $\phi = 1.2$, when ϕ decreases, there is a value of ϕ (for a specific H_2%) triggering a sharp decrease of the emissions and marking the transition from flame Type I to flame Type II. Therefore, like in the previous section, the analysis starts by flame Type I, followed by flame Type II. Hydrogen's effect is addressed in the discussion of each flame type.

Flame Type I

Consider, again, the range of ϕ of flame Type I, according to each H_2%. Starting from the lower equivalence ratios, there is a general decrease of NO_x emissions with ϕ until, $\phi = 1$. Previous studies [6, 7, 31] show that temperatures inside IDF under fuel-lean conditions are less than 1800 K, which cannot provide enough energy to activate the thermal-NO (Zeldovich) mechanism [5]. In the previous section, it was

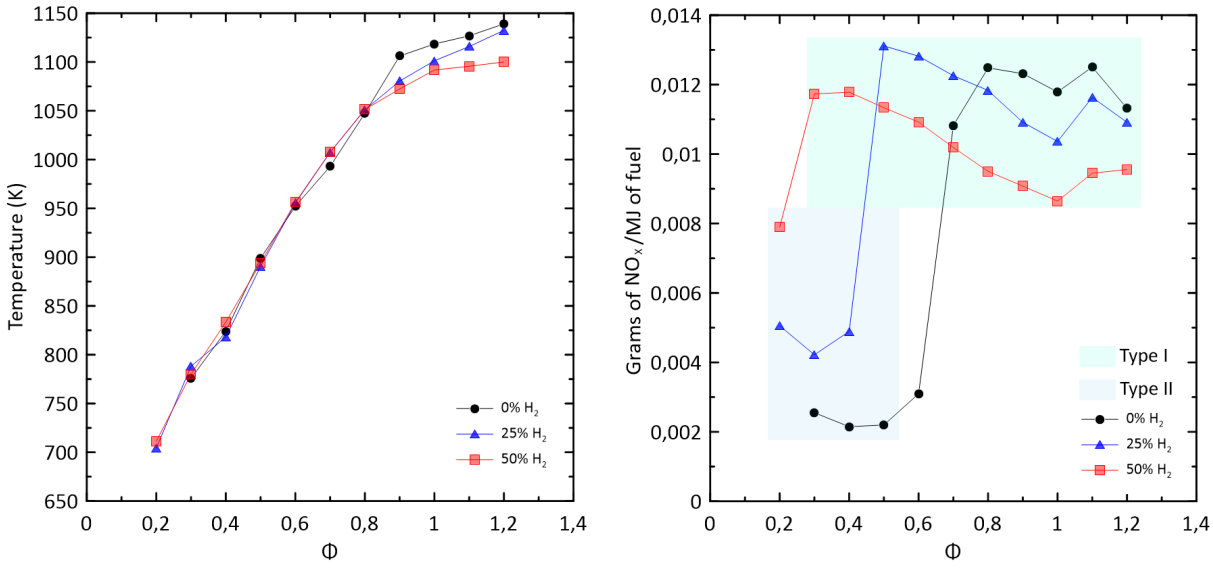

(a) Temperature.

(b) NO_x.

Figure 3.12: Variation of NO_x emissions and temperature of the flue gases with ϕ for 0%, 25% and 50% of H_2. Highlighted sections of the plots correspond to emissions of flames Type I and II.

reported that UHC emissions increase as Re_{air} also increases. The increase of UHC emissions, as stated before, is associated to incomplete combustion. Hence, its increase is associated to the rise of CH radicals in the flame, which can initiate the Fenimore mechanism [5]. Therefore, for flame Type I, NO_x emissions are higher for lower equivalence ratios, just like with UHC emissions in flame Type I. When ϕ increases from $\phi = 0.3$ (50%H_2), $\phi = 0.5$ (25%H_2) and $\phi = 0.8$ (0%H_2) to $\phi = 1$, NO_x emissions tend to decay since the same happens with UHC - when UHC emissions decrease, combustion tends to be more complete and the amount of CH radicals in the flame decreases, impeding the formation of NO_x by the Fenimore mechanism. Moreover, if one focus on the NO_x emissions from stoichiometric conditions towards leaner conditions, the noticeable increase in NO_x emissions is accompanied by an evident decrease in temperature, as suggested by Figures 3.12 (b) and (a), respectively. These opposite transitions suggest that the Fenimore mechanism might be predominant in this range of ϕ, rather than the thermal-NO (Zeldovich) mechanism. When ϕ further increases, from stoichiometric conditions, NO_x emissions slightly increase. Miao et al. [48] also reported a decrease of NO_x emissions from $\phi = 0.3$ to $\phi = 0.7$, and a further increase for richer conditions due to temperature rising which activates the Zeldovich mechanism and increases NO_x emissions.

As Figure 3.12 (b) illustrates, in general, hydrogen addition tends to decrease the the amount of NO_x emitted for flame Type I. Increasing H_2% on the fuel slightly decreases NO_x emissions from 0%H_2 to 25%H_2. From 25%H_2 to 50%H_2 that decrease is higher and more uniform. As stated before, for $\phi \leq 1$, NO_x emissions seem to be dominated by the Fenimore mechanism. As hydrogen is added to flame Type I, the carbon content of the fuel reduces, reducing, in turn, the CH radicals produced. If CH radicals are reduced, the same happens to the NO_x emissions linked to the Fenimore mechanism. For $\phi \geq 1$, even though Zeldovich mechanism comes into play, Fenimore mechanism still has importance [5]. Therefore, the reduction of the carbon content of the fuel by the hydrogen addition will also reduce the NO_x emis-

sions for $\phi \geq 1$.

Flame Type II

Recall the range of ϕ of flame Type II, according to each H_2%. As transformation from flame Type I to Type II takes place, most of FRA Type I extinguishes. As mentioned in section 3.1, FRA Type I has higher area and is more luminous than FRA Type II. Therefore, the amount of carbon fuel in combustion is higher (more tendency to form CH radicals) and the mixing quality of the reactants of FRA Type I is much better than FRA Type II. CH radicals, and NO_x from the Fenimore mechanism, are produced in the flame zone where mixture quality of reactants is better [5]. Hence, NO_x formation ways linked to the production of CH radicals vanish and NO_x emissions slump.
For flame Type II, in contrast to flame Type I, NO_x emissions increase with the H_2%. As it was explained for the effect of hydrogen on the emissions of UHC and CO from flame Type II, H_2 addition will increase the reaction rate and the amount of fuel under combustion, i.e., increasing the H_2% will increase the amount of fuel ignited. When more fuel is ignited, the amount of CH radicals increases and so do the NO_x emissions from the Fenimore mechanism.

3.4 Overview

This final section presents an overview of the discussion carried out in the previous sections. Based on its structures, two main flame types were identified and hydrogen, when added to the fuel, does not create new ones. The main difference between these two flame structures is the FRA of each one. Flame Type I has a luminous FRA, with considerable area, anchored to the burner and with high reaction rate. The vertical velocity profile and the flow field of this flame are broader than those of flame Type II, since FRA is anchored right at the exit of the slits. Due to the characteristics of FRA Type I just mentioned, most of the fuel is burned and combustion is virtually complete within the equivalence ratio ranges of this flame type. Therefore, CO_2 emissions are higher and CO and UHC emissions are almost null. However, even under near stoichiometric conditions, a regular (very small) mass of UHC keeps being emitted. Furthermore, the PIV analysis suggests that a central fraction of the air jet escapes combustion (between the two FRA). These two observations are in accordance and suggest that some fuel is diffused into the central fraction of the air jet that escapes combustion. The emissions of NO_x seem to be dominated by the Fenimore mechanism for $\phi \leq 1$, with increasing values towards leaner conditions, in accordance with the increasing UHC emissions. In parallel with the increasing NO_x emissions, temperature decreases, also suggesting that the thermal-NO mechanism is less predominant than the Fenimore mechanism.
By increasing the mass flow rate of the central air jet, an increasing shear lifting force, combined with an increasing momentum of the air jet, starts affecting the flame structure. FRA Type II is formed, stabilized in a higher position, with notably smaller area and less luminosity than FRA Type I. The flow field and velocity profiles of flame Type II are narrower than those of flame Type I, due to lower combustion area,

which results in smaller temperatures and less expansion of the gases that take part in the combustion process. The emission behavior of this flame type is much different from its counterpart. Characteristic velocities associated with this flame are higher, hence, residence times are lower and combustion is incomplete. The emissions of CO and UHC, products of incomplete combustion, soar as Re_{air} increases. The velocity vector map of the flow field of flame Type II reveals that a much bigger fraction of the central air jet, in comparsion to flame Type I, escapes combustion in between the two FRAs. This is also in accordance with the escalating amount of UHC emitted, possibly entrained by the big fraction of air that escapes combustion. Naturally, as combustion gets poorer and CO and UHC emissions increase, CO_2 emissions become lower for flame Type II. Regarding the NO_x emissions, as FRA Type I vanishes, the amount of CH radicals produced reduces, resulting in reduced NO_x emissions for flame Type II.

Regarding the flame structure, when hydrogen is added to the fuel, its unique properties - low density and high thermal diffusivity - decrease the ignition energy of the fuel and increase the reaction rate. Considering the case in which flame Type II becomes Type I, the increased reaction rate of FRA Type II, combined with the lower ignition energy of the fuel, will ignite most of the portion of air and fuel previously escaping combustion and form FRA Type I. If hydrogen is added to the fuel feeding a Type I flame, flame morphology does not change. However, flame length and width reduce, due to increased reaction rate, and flame luminosity decays.

Hydrogen's impact on the emission behavior of the flames herein studied is a more complex subject. The H_2% on the fuel blend has a direct impact on flue gas emissions by reducing the carbon content of the fuel. For flame Type I, CO_2 emissions show a significant decrease, whereas CO and UHC show very small, almost negligible reductions, since its emissions were already almost null, without H_2. As the carbon content of the fuel decays, the CH radicals produced within the flame also decay and NO_x emissions linked to the Fenimore mechanism are also slightly reduced when H_2% increases. For the case of flame Type II, the direct impact of the fuel's hydrogen content is also a reduction of the carbon related emissions, and an increase of NO_x emissions. However, besides this direct impact on the emissions of each flame type, H_2% on the fuel causes an indirect impact on those emissions too. As mentioned before, increasing H_2% on the fuel increases the range in which flame Type I holds stable. Flame Type I presents considerable differences in terms of the flue gas composition when compared to flame Type II, i.e., flue gas composition is very much affected by the flame type. Therefore, by promoting an extended equivalence ratio range for flame Type I, H_2 addition to the fuel blend enables an extended range of ϕ in which emissions from flame Type I, which is more efficient than flame Type II, predominate.

Combining the direct and indirect influences of the fuel's hydrogen content on the emission pattern of the flames studied, increasing H_2% enables the presence of an efficient flame (Type I), with almost negligible UHC and CO emitted and reduced emissions of CO_2 and NO_x, under ultra-lean conditions. Table 3.1 compares the overall emissions from flames Type I and Type II for a certain hydrogen percentage on the fuel blend. E_I and E_{II} stand for emissions from flames Type I and Type II, respectively, in grams of emitted gas per MJ of fuel supplied. Table 3.2 summarizes the direct effects of the hydrogen dose of the fuel blend on the emissions from both flames studied. N.E. stands for no effect. Notice that, for CO emissions from flame Type I, even if the decrease is very small, it exists, as mentioned before.

Table 3.1: Comparison of UHC, CO, CO_2 and NO_x emissions between flame Type I and Type II, for a fixed H_2%.

UHC	**CO**	**CO_2**	**NO_x**
$E_I \leq E_{II}$	$E_I \leq E_{II}$	$E_I \geq E_{II}$	$E_I \geq E_{II}$

Table 3.2: Summary of H_2% effect on pollutant emissions from UHC, CO, CO_2 and NO_x.

Flame	**UHC**	**CO**	**CO_2**	**NO_x**
Type I	N.E.	Decrease	Decrease	Decrease
Type II	Decrease	Decrease	Decrease	Increase

Chapter 4

Conclusions

4.1 Achievements

The two main goals of this work were to characterize the impact of fuel's hydrogen content on the flame structure and emission characteristics, under fuel-lean conditions. To achieve this, a working range of stable flames was established. Global equivalence ratio varied from 0.2 to 1.2 and hydrogen content of the fuel was set at 0%, 25% and 50%H_2 by volume. For each H_2%, equivalence ratio and, hence, velocity ratio, was varied by varying Re_{air}. Power supplied to the flame kept at a constant value of 236 W. By means of flame photography to the whole flame range, two main structures were identified and described. The impact of H_2 on the IDF morphology was also discussed. To understand the characteristics of the flow field associated with each flame structure and how hydrogen affects it, a PIV analysis was performed. For the two flame structures, velocity vector maps and velocity profiles, at the base and top of the flame, were obtained and discussed. With the purpose of understanding how were emissions of these IDF affected by hydrogen, an extensive analysis of the flue gases from the flame was conducted. Namely emissions of UHC, CO_2, CO and NO_x were analyzed for the whole range of flames studied. Temperature of the flue gases was also measured in order to help understanding the underlying mechanisms of NO_x formation. An overview correlating the results obtained and its discussions was accomplished Section 3.4. A summary of the most important findings of this thesis is presented below:

1. Based on its structure, two distinct flame types were identified, with two main flame regions: an inner flame region, FRA, where fuel burns with the central air jet and an outer flame region, FRB, where fuel burns with the exterior air. Flame Type I exhibits a luminous FRA, with considerable area and anchored to the top of the burner. Flame Type II is characterized by a smaller and less luminous FRA, stabilized in a higher position than FRA Type I.

2. Hydrogen addition to the fuel blend does not create new flame structures, in agreement with the results obtained by Miao et al. [46]. However, when H_2% is increased, the range of ϕ in which flame Type I holds stable is increased towards leaner conditions and the opposite trend is verified for flame Type II.

3. Addition of hydrogen to the fuel blend increases stability of flame Type I and reduces its length, width and luminosity. For flame Type II, hydrogen addition changes its structure, turning it into flame Type I - FRA Type II increases its area and luminosity and adheres to the top of the burner, becoming an FRA Type I.

4. PIV analysis of both flame types reveals broader velocity profiles and flow fields of flame Type I than flame Type II. Furthermore, flame Type II features a significant portion of the air jet escaping combustion. The same phenomena is verified for flame Type I but on a much smaller scale.

5. Flame Type I reports very low or null emissions of CO and UHC and higher CO_2 emissions. Emissions of CO and UHC soar as flame Type II is formed and CO_2 emissions drop. These observations suggest that flame Type II is more inefficient than flame Type I.

6. Flame Type I presents a growing trend of NO_x emissions towards leaner conditions, possibly associated with the Fenimore mechanism. As flame Type II is formed and FRA Type I vanishes, NO_x emissions slump. A linear temperature decrease in parallel with increasing NO_x emissions also suggests that the Zeldovich mechanism, apparently, is not predominant.

7. For both flame types, hydrogen addition reduces the carbon related emissions: CO_2 verifies considerable reductions and smaller reductions are reported for UHC and CO. Overall efficiency of the flame, apparently, is not much affected by H_2 on the fuel blend. Emissions of NO_x for flame Type I decrease as H_2% is increased; the opposite trend is verified for flame Type II.

8. Emission characteristics of each flame configuration are mainly affected by the flame structure and H_2% on the fuel. By extending the equivalence ratio range in which flame Type I holds stable, hydrogen addition enables the presence of an efficient flame (Type I) with very low or null emissions of UHC and CO and reduced emissions of CO_2 and NO_x, under ultra-lean conditions.

4.2 Future Work

The work developed in this dissertation provides an extensive investigation on the characterization of hydrogen enriched methane IDF, under fuel-lean conditions. Even so, this work points to further research regarding temperature and chemiluminescence analysis and testing of new fuel blends:

1. Being a diffusion flame, spatial temperature gradients of this IDF are expected to be high. Furthermore, it is not clear what is the main NO_x formation mechanism near stoichiometric conditions. Therefore, a numerical simulation of the temperature of the flame over its area, and for the same conditions studied in this work, would be of great interest.

2. Due to the highly heterogeneous nature of the mixing phenomena of this flame, local equivalence ratios within the the flame are highly variable [34]. Consequently, by means of an analysis of the chemiluminescent emissions of CH^* and OH^*, the impact of H_2 on the local equivalence ratio may be studied and correlated with the numerical results obtained for temperature.

3. Besides hydrogen, another fuel that is receiving much attention by the combustion industry is biogas. It would be of substantial interest to understand the impact of adding CO_2 to the fuel blend in the flame structures and emissions obtained herein.

Bibliography

[1] NASA. Global climate change - vital signs of the planet. 2019. URL https://climate.nasa.gov/evidence/.

[2] I. E. A. IEA. World energy outlook - the gold standard of energy analysis. 2019. URL https://www.iea.org/weo/.

[3] BP. BP Energy Outlook 2019 edition The Energy Outlook explores the forces shaping the global energy transition out to 2040 and the key uncertainties surrounding that. Technical report, 2019.

[4] I. E. A. IEA. World energy investment 2019 - investing in our energy future. 2019. URL https://www.iea.org/wei2019/end-use/.

[5] S. R. Turns. *An Introduction to Combustion Concepts and Applications*. McGraw-Hill, 3 edition, 2012.

[6] L. K. Sze, C. S. Cheung, and C. W. Leung. Temperature distribution and heat transfer characteristics of an inverse diffusion flame with circumferentially arranged fuel ports. *International Journal of Heat and Mass Transfer*, 47(14-16):3119–3129, 2004. ISSN 00179310.

[7] L. L. Dong, C. S. Cheung, and C. W. Leung. Heat transfer characteristics of an impinging inverse diffusion flame jet - Part I: Free flame structure. *International Journal of Heat and Mass Transfer*, 50(25-26):5108–5123, 2007. ISSN 00179310.

[8] J. Miao, C. W. Leung, and C. S. Cheung. Effect of hydrogen percentage and air jet Reynolds number on fuel lean flame stability of LPG-fired inverse diffusion flame with hydrogen enrichment. *International Journal of Hydrogen Energy*, 39(1):602–609, 2014. ISSN 03603199.

[9] Shell. Shell hydrogen study, energy of the future? sustainable mobility through fuel cells and hydrogen. 2019. URL https://www.shell.com/energy-and-innovation/new-energies/hydrogen/_jcr_content/par/keybenefits_150847174/link.stream/1496312627865/6a3564d61b9aff43e087972db5212be68d1fb2e8/shell-h2-study-new.pdf.

[10] I. E. A. IEA. Hydrogen a key part of a clean and secure energy future. 2019. URL https://www.iea.org/topics/hydrogen/production/.

[11] E. Hu, Z. Huang, J. He, C. Jin, and J. Zheng. Experimental and numerical study on laminar burning characteristics of premixed methane–hydrogen–air flames. *International Journal of Hydrogen Energy*, 34(11):4876 – 4888, 2009. ISSN 0360-3199. 2nd International Workshop on Hydrogen.

[12] F. Halter, C. Chauveau, and I. Gökalp. Characterization of the effects of hydrogen addition in premixed methane/air flames. *International Journal of Hydrogen Energy*, 32(13):2585 – 2592, 2007. ISSN 0360-3199. ICHS-2005.

[13] E. C. Okafor, A. Hayakawa, Y. Nagano, and T. Kitagawa. Effects of hydrogen concentration on premixed laminar flames of hydrogen–methane–air. *International Journal of Hydrogen Energy*, 39 (5):2409 – 2417, 2014. ISSN 0360-3199.

[14] A. R. Choudhuri and S. Gollahalli. Combustion characteristics of hydrogen–hydrocarbon hybrid fuels. *International Journal of Hydrogen Energy*, 25(5):451 – 462, 2000. ISSN 0360-3199.

[15] A. R. Choudhuri and S. Gollahalli. Characteristics of hydrogen–hydrocarbon composite fuel turbulent jet flames. *International Journal of Hydrogen Energy*, 28(4):445 – 454, 2003. ISSN 0360-3199.

[16] S. El-Ghafour, A. El-dein, and A. Aref. Combustion characteristics of natural gas–hydrogen hybrid fuel turbulent diffusion flame. *International Journal of Hydrogen Energy*, 35(6):2556 – 2565, 2010. ISSN 0360-3199.

[17] K. Zhao, D. Cui, T. Xu, Q. Zhou, S. Hui, and H. Hu. Effects of hydrogen addition on methane combustion. *Fuel Processing Technology*, 89(11):1142 – 1147, 2008. ISSN 0378-3820.

[18] M. Reyes, F. Tinaut, B. Giménez, and J. V. Pastor. Effect of hydrogen addition on the oh* and ch* chemiluminescence emissions of premixed combustion of methane-air mixtures. *International Journal of Hydrogen Energy*, 43(42):19778 – 19791, 2018. ISSN 0360-3199.

[19] J. Arthur and D. Napier. Formation of carbon and related materials in diffusion flames. *Symposium (International) on Combustion*, 5(1):303 – 316, 1955. ISSN 0082-0784.

[20] K.-T. Wu and R. H. Essenhigh. Mapping and Structure of Inverse Diffusion Flames of Methane. *Proceedings of the Combustion Institute*, 20:1925–1932, 1984.

[21] K.-T. Wu and R. H. Essenhigh. Mapping and structure of inverse diffusion flames of methane. *Symposium (International) on Combustion*, 20(1):1925 – 1932, 1985. ISSN 0082-0784. Twentieth Symposium (International) on Combustion.

[22] C. R. Shaddix, T. C. Williams, L. G. Blevins, and R. W. Schefer. Flame structure of steady and pulsed sooting inverse jet diffusion flames. *Proceedings of the Combustion Institute*, 30(1):1501–1508, 2005. ISSN 15407489.

[23] M. A. Mikofski, T. C. Williams, C. R. Shaddix, A. C. Fernandez-Pello, and L. G. Blevins. Effect of varied air flow on flame structure of laminar inverse diffusion flames. 2004.

[24] M. A. Mikofski, T. C. Williams, C. R. Shaddix, A. C. Fernandez-Pello, and L. G. Blevins. Structure of laminar sooting inverse diffusion flames. *Combustion and Flame*, 146, 2006.

[25] M. A. Mikofski, T. C. Williams, C. R. Shaddix, A. C. Fernandez-Pello, and L. G. Blevins. Structure of laminar sooting inverse diffusion flames. *Combustion and Flame*, 149(4):463–478, 2007. ISSN 00102180.

[26] L. K. Sze, C. S. Cheung, and C. W. Leung. Appearance, temperature, and NOx emission of two inverse diffusion flames with different port design. *Combustion and Flame*, 144(1-2):237–248, 2006. ISSN 00102180.

[27] L. Dong, C. Cheung, and C. Leung. Heat transfer characteristics of an impinging inverse diffusion flame jet. part ii: Impinging flame structure and impingement heat transfer. *International Journal of Heat and Mass Transfer*, 50(25):5124 – 5138, 2007. ISSN 0017-9310.

[28] A. Sobiesiak and J. C. Wenzell. Characteristics and structure of inverse flames of natural gas. *Proceedings of the Combustion Institute*, 30(1):743 – 749, 2005. ISSN 1540-7489.

[29] A. M. Elbaz and W. L. Roberts. Flame structure of methane inverse diffusion flame. *Experimental Thermal and Fluid Science*, 56:23–32, 2014. ISSN 08941777.

[30] H. S. Zhen, Y. S. Choy, C. W. Leung, and C. S. Cheung. Effects of nozzle length on flame and emission behaviors of multi-fuel-jet inverse diffusion flame burner. *Applied Energy*, 88(9):2917–2924, 2011. ISSN 03062619.

[31] L. L. Dong, C. S. Cheung, and C. W. Leung. Combustion optimization of a port-array inverse diffusion flame jet. *Energy*, 36(5):2834–2846, 2011. ISSN 03605442.

[32] H. Zhen, C. Leung, and C. Cheung. Thermal and emission characteristics of a turbulent swirling inverse diffusion flame. *International Journal of Heat and Mass Transfer*, 53(5):902 – 909, 2010. ISSN 0017-9310.

[33] H. Zhen, C. Leung, and C. Cheung. A comparison of the thermal, emission and heat transfer characteristics of swirl-stabilized premixed and inverse diffusion flames. *Energy Conversion and Management*, 52(2):1263 – 1271, 2011. ISSN 0196-8904.

[34] M. Ribeiro, F. Quintino, and E. Fernandes. Characterization of methane inverse diffusion flames in a multi-slot burner, 2019.

[35] Y. Zhang, J. Wu, and S. Ishizuka. Hydrogen addition effect on laminar burning velocity, flame temperature and flame stability of a planar and a curved ch4–h2–air premixed flame. *International Journal of Hydrogen Energy*, 34(1):519 – 527, 2009. ISSN 0360-3199.

[36] P. Kumar and D. Mishra. Experimental investigation of laminar lpg–h2 jet diffusion flame. *International Journal of Hydrogen Energy*, 33(1):225 – 231, 2008. ISSN 0360-3199. IWHE 2006.

[37] L. Wu, N. Kobayashi, Z. Li, H. Huang, and J. Li. Emission and heat transfer characteristics of methane–hydrogen hybrid fuel laminar diffusion flame. *International Journal of Hydrogen Energy*, 40(30):9579 – 9589, 2015. ISSN 0360-3199.

[38] E. Hu, Z. Huang, J. He, and H. Miao. Experimental and numerical study on lean premixed methane–hydrogen–air flames at elevated pressures and temperatures. *International Journal of Hydrogen Energy*, 34(16):6951 – 6960, 2009. ISSN 0360-3199. 4th Dubrovnik Conference.

[39] Z. Li, X. Cheng, W. Wei, L. Qiu, and H. Wu. Effects of hydrogen addition on laminar flame speeds of methane, ethane and propane: Experimental and numerical analysis. *International Journal of Hydrogen Energy*, 42(38):24055 – 24066, 2017. ISSN 0360-3199.

[40] J. Liu, X. Zhang, T. Wang, X. Hou, J. Zhang, and S. Zheng. Numerical study of the chemical, thermal and diffusion effects of h2 and co addition on the laminar flame speeds of methane–air mixture. *International Journal of Hydrogen Energy*, 40(26):8475 – 8483, 2015. ISSN 0360-3199.

[41] L. Gülder, D. Snelling, and R. Sawchuk. Influence of hydrogen addition to fuel on temperature field and soot formation in diffusion flames. *Symposium (International) on Combustion*, 26(2):2351 – 2358, 1996. ISSN 0082-0784.

[42] Z. Sun, B. Dally, G. Nathan, and Z. Alwahabi. Effects of hydrogen and nitrogen on soot volume fraction, primary particle diameter and temperature in laminar ethylene/air diffusion flames. *Combustion and Flame*, 175:270 – 282, 2017. ISSN 0010-2180. Special Issue in Honor of Norbert Peters.

[43] H. J. Burbano, A. A. Amell, and J. M. García. Effects of hydrogen addition to methane on the flame structure and co emissions in atmospheric burners. *International Journal of Hydrogen Energy*, 33 (13):3410 – 3415, 2008. ISSN 0360-3199. 2nd National and 1st Latin American Congress, Hydrogen and Sustainable Energy Sources.

[44] C. Ji and S. Wang. Effect of hydrogen addition on combustion and emissions performance of a spark ignition gasoline engine at lean conditions. *International Journal of Hydrogen Energy*, 34(18):7823 – 7834, 2009. ISSN 0360-3199.

[45] H. S. Kim, V. K. Arghode, M. B. Linck, and A. K. Gupta. Hydrogen addition effects in a confined swirl-stabilized methane-air flame. *International Journal of Hydrogen Energy*, 34(2):1054 – 1062, 2009. ISSN 0360-3199.

[46] J. Miao, C. W. Leung, C. S. Cheung, and R. C. K. Leung. Flame Stability and Structure of Liquefied Petroleum Gas-Fired Inverse Diffusion Flame with Hydrogen Enrichment. 7(1):616–621, 2013.

[47] J. Miao, C. W. Leung, C. S. Cheung, Z. Huang, and W. Jin. Effect of H2 addition on OH distribution of LPG/Air circumferential inverse diffusion flame. *International Journal of Hydrogen Energy*, 41 (22):9653–9663, 2016. ISSN 03603199.

[48] J. Miao, C. W. Leung, C. S. Cheung, Z. H. Huang, and H. S. Zhen. Effect of hydrogen addition on overall pollutant emissions of inverse diffusion flame. *Energy*, 104:284–294, 2016. ISSN 03605442.

[49] V. de Brederode. *Aerodinâmica Incompressível: Fundamentos*. IST Press, 1 edition, 2014. ISBN 978-989-8481-32-0.

[50] S. Mahesh and D. P. Mishra. Flame structure of LPG-air Inverse Diffusion Flame in a backstep burner. *Fuel*, 89(8):2145–2148, 2010. ISSN 00162361.

[51] F. P. Incropera, D. P. Dewitt, T. L. Bergman, and A. S. Lavine. *Fundamentals of Heat and Mass Transfer*. J. Wiley & Sons, 6 edition, 2007. ISBN 9780470501979.

[52] R. J. M. Bastiaans. *Cross-correlation PIV : theory , implementation and accuracy Cross-correlation PIV ; theory , implementation and accuracy Department of Mechanical Engineering , Section of Internal Combustion Engines , Eindhoven University of Technology ,*. Number January 2000. 2014. ISBN 903862851X.

[53] K. Okamoto, S. Nishio, T. Saga, and T. Kobayashi. Standard images for particle-image velocimetry. *Measurement Science and Technology*, 11(6):685–691, may 2000.

[54] M. Raffel, C. E. Willert, S. T. Wereley, and J. Kompenhans. *Particle Image Velocimetry - A Pratical Guide*. Springer, 1998. ISBN 9783540723073.

[55] A. Melling. Tracer particles and seeding for particle image velocimetry. *Measurement Science and Technology*, 8(12):1406–1416, dec 1997.

[56] Dantec Dynamics. User's Guide Dynamic Studio, 2016.

[57] B. Zhang, C., Vasilevskis, S., & Kozlowski. Particle Image Velocimetry: User Guide. page 35, 2018.

[58] K. Kiger. PIV Basics: Correlation. In *SEDITRANS summer school on Measurement techniques for turbulent open-channel flows*, 2015.

[59] Y. S. Choy, H. S. Zhen, C. W. Leung, and H. B. Li. Pollutant emission and noise radiation from open and impinging inverse diffusion flames. *Applied Energy*, 91(1):82–89, 2012. ISSN 03062619.

[60] W. G. S. Hugh W. Coleman. *Experimentation, Validation, and Uncertainty Analysis for Engineers*. J. Wiley & Sons, 4 edition, 2018. ISBN 1119417708, 9781119417705.

[61] E. W. Lemmon, R. T. Jacobsen, S. G. Penoncello, and D. G. Friend. Thermodynamic properties of air and mixtures of nitrogen, argon, and oxygen from 60 to 2000 k at pressures to 2000 mpa. *Journal of Physical and Chemical Reference Data*, 29(3):331–385, 2000.

[62] D. Bradley and K. J. Matthews. Measurement of high gas temperatures with fine wire thermocouples. *Journal of Mechanical Engineering Science*, 10(4):299–305, 1968.

[63] D. Mishra and P. Kumar. Experimental investigation of laminar lpg–h2 jet diffusion flame with preheated reactants. *Fuel*, 87(13):3091 – 3095, 2008. ISSN 0016-2361.

[64] F. Coppens, J. D. Ruyck, and A. Konnov. The effects of composition on burning velocity and nitric oxide formation in laminar premixed flames of ch4 + h2 + o2 + n2. *Combustion and Flame*, 149(4): 409 – 417, 2007. ISSN 0010-2180.

[65] C. Fotache, T. Kreutz, and C. Law. Ignition of hydrogen-enriched methane by heated air. *Combustion and Flame*, 110(4):429 – 440, 1997. ISSN 0010-2180.

[66] A. M. Elbaz and W. L. Roberts. Experimental characterization of methane inverse diffusion flame. *Combustion Science and Technology*, 186(9):1249–1272, 2014. ISSN 1563521X.

Appendix A

Publications

This work was presented in an international conference, in which it was selected for a special issue of the Fuel journal:

- **F. M. Vaz**, F. M. Quintino, E. C. Fernandes. "Characterization of the impact of H_2 on CH_4/air inverse diffusion flames", in *Clean Air 2019 - 14th International Conference on Energy for a Clean Environment*, Funchal, Madeira (Portugal), September 8-12, 2019.